An analytical model to predict strain-hardening behaviour and twin volume fraction in a profoundly twinning magnesium alloy

Sudeep Sahoo, Laszlo Toth, Somjeet Biswas

An analytical model to predict strain-hardening behaviour and twin volume fraction in a profoundly twinning magnesium alloy

Sudeep K Sahoo[1], Laszlo S Toth[2, 3], Somjeet Biswas[1]

[1]Department of Metallurgical and Materials Engineering, Indian Institute of Technology Kharagpur, West Bengal 721302, India

[2]Laboratoire d'Etude des Microstructures de Mécanique des Matériaux (LEM3), CNRS UMR 7239, Université de Lorraine, 57045 Metz Cedex 1, France

[3]Laboratory of Excellence on Design of Alloy Metals for low-mAss Structures (DAMAS), Université de Lorraine, Metz, France

Abstract

An analytical model is presented that can successfully predict the strain hardening behaviour as well as the variations in twin volume fraction in polycrystalline Magnesium alloy Mg-3Al-0.3Mn that twins profoundly during deformation. The model is composed of three basic elements: (i) Twin fraction prediction, based on crystal plasticity elements, (ii) a two-phase composite model composed of the matrix and the twins by adopting the "Iso-work" hypothesis, (iii) a strain hardening approach inspired from a crystal plasticity model. The experiments include uniaxial compression tests for two different cases at ambient temperature. The microstructures were characterized at various strains up to fracture using the Electron Back-Scattered Diffraction technique in a FEG-SEM. The microstructural investigation revealed the formation of a lamellar structure of alternated layers of matrix and $\{10\bar{1}2\}\langle 10\bar{1}\bar{1}\rangle$-extension twin domains. With progressive deformation, the twins broadened and consumed the entire microstructure prior to fracture. The model could accurately reproduce the experimental twin-induced sigmoidal shaped flow curve together with the twin volume fraction evolution.

Keywords: Magnesium alloy; Strain Hardening Behaviour; Deformation Twinning; Plastic deformation; Electron Back-Scattered Diffraction

Corresponding author: Laszlo S. Toth, Laszlo.toth@univ-lorraine.fr

1. Introduction

Hexagonal closed packed (hcp) Magnesium (Mg) alloys are considered as future materials for automobiles and aircraft applications (Biswas et al., 2013; Joost and Krajewski, 2017). However, their application potential is restricted mainly due to their limited strength and ductility at ambient temperature. To successfully implement Mg alloys in application, a comprehensive understanding of the deformation behaviour is required by means of consecutive experimental and modelling/simulation studies. In this aspect, the mechanisms underlying the plastic deformation of polycrystalline Mg alloys had been widely explored in recent years (Graff et al., 2007; Barnett et al., 2004; Biswas et al., 2010, 2013; Beausir et al., 2009; Cáceres et al., 2008; Gu et al., 2013; Khan et al., 2011; Levinson et al., 2013; Lou et al., 2007; Mu et al., 2014; Yoo, 1981). Studies on the deformation behaviour of polycrystalline Mg alloys frequently report deformation twins (Biswas et al., 2010, 2013; Beausir et al., 2009; Gu et al., 2013; Knezevic et al., 2010; Levinson et al., 2013), that include $\{10\bar{1}2\}\langle 10\bar{1}\bar{1}\rangle$ extension twins and $\{10\bar{1}1\}\langle 10\bar{1}\bar{2}\rangle$ contraction twins. As the names imply, the extension twinning mode accommodates tensile strain along the crystallographic c-axis, whereas the contraction twinning mode produces compressive strain along the same. These two twinning modes are associated in Mg with a shear strain of 0.1289 and 0.1377, reorienting the crystal lattice about the $\langle 11\bar{2}0\rangle$ axis by ~86.3° and by ~56.2°, respectively (Ardeljan et al., 2016; Christian and Mahajan, 1995; Knezevic et al., 2010; Niewczas et al., 2010; Yoo, 1981). Therefore, depending upon the deformation conditions, the activation of twin systems plays a significant role in texture reorientation (Ando et al., 2014; Barnett et al., 2004; Cáceres et al., 2008; Gu et al., 2013; Khan et al., 2011; Lou et al., 2007; Mu et al., 2014; Yoo, 1981), strain-hardening (Cáceres et al., 2008; Knezevic et al., 2010; Mu et al., 2014) and in most cases, it results in fracture (Ando et al., 2014; Fernández et al., 2011; Yoo, 1981).

It is widely understood that the observed strain hardening behaviour helps in deciphering deformation mechanisms. The most conventional approach for studying the strain hardening effect is simple compression or tension testing. Studies on Mg alloys have illustrated the profuse activity of $\{10\bar{1}2\}$ twins during deformation at low homologous temperatures. Indeed, the occurrence of extension twins is often characterized by a sigmoidal shaped flow curve (Guo

et al., 2015; Khan et al., 2011; Mu et al., 2011, 2014; Lou et al., 2007; Barnett et al., 2004). The deformation twin-induced strain hardening characteristics can be attributed to:

(i) Formation of twin-induced special boundaries within grains, known as coincidence site lattice (CSL) boundaries (Lay et al., 1992; Hu and Randle, 2007) that may lead to Hall-Petch like hardening (Proust et al., 2009; Salem et al., 2003). However, in Mg single phase alloys, minimal Hall-Petch hardening due to extension twins was identified (Dixit et al., 2015; Jain and Agnew, 2007; Knezevic et al., 2010). It was reported that the rapid growth of the twinned domain encompasses the entire parent grain without imposing appreciable barrier effect to slip (Knezevic et al., 2010). Lou et al. (2007) have witnessed that in AZ31B, transmission of dislocations through extension twin boundaries occurs easily, leading to negligible Hall-Petch type hardening effect.

(ii) Basinski type hardening (Basinski et al., 1997) may occur as a result of transmutation of glissile to sessile dislocations from the parent matrix into twin domains (Clausen et al., 2008; Jahedi et al., 2017; Knezevic et al., 2012, 2015; Zhang and Joshi, 2012). Wang and Agnew (2016) presented a detailed TEM analysis of dislocation transmutation in AZ31 alloy. They showed that very high dislocation densities can develop near the twin phase boundaries. On the other hand, Zilahi (2018) measured dislocation densities by synchrotron x-ray line profile analysis in many grains of compressed AZ31 Mg and found higher dislocation densities in the extension twins. Allen et al. (2018) presented a successful hardening model based on dislocation transmutation between the matrix and twin phases, implemented into the VPSC model.

(iii) Extension twinning in Mg and its alloys leads to abrupt crystal reorientation with respect to the parent grain. Stohr et al. (1972) and Obara et al. (1973) pointed out high strain-hardening rate associated with c-axis compression in Mg. Agnew et al. (2002) reported that significant stress concentration is required to activate extension twins. Concurrently, by using neutron diffraction experiments Agnew et al. (2003) showed that the apparent strain hardening is actually due to composite-like load sharing between the softer parent matrix and the harder extension twin oriented domains. Wang et al. (2012) demonstrated that texture strengthening is primarily due to the formation of extension twins leading to an increase in strain hardening rate in Stage-II of the flow curve. Thus, the phenomenon of textural hardening is primarily

attributed to extension twin-induced reorientation as suggested by several researchers (Dixit et al., 2015; Jain and Agnew, 2007; Jiang et al., 2007; Knezevic et al., 2010; Lou et al., 2007).

The above aspects provide that the mechanical response of the matrix and the twin phase can be dissimilar due to their orientation difference. This could strongly influence the strain hardening response of the individual phases. Additionally, the combined strain hardening behaviour must be influenced by their respective volume fractions.

It is important to provide analytical approaches that can readily predict the changes in strain hardening due to twinning. Five such models were presented so far (Barnett et al., 2005, 2015; Bouaziz and Guelton, 2001; Fullman, 1953; Karaman et al., 2000). Fullman (1953) linked the twin lamella thickness to the twin volume fraction and then used a Taylor kind of equation to obtain the stress-strain relation. In their approach, the twin volume fraction cannot be predicted rather it had to be provided as a function of strain. Further, Bouaziz and Guelton (2001) introduced an empirical relation for the twin volume fraction by considering the creation and annihilation of dislocations. A more complete model was proposed for TWIP steel in cyclic loading by Karaman et al. (2000), where both isotropic and kinematic hardening were considered to describe the high Bauschinger effect. Barnett et al. (2005) proposed a model in which a parameter (i.e. twin fraction) was introduced to describe the difference in the stress-strain response for twinning and non-twinning-dominated deformation conditions. In their work, Mg single crystal was tested under tension where no twinning occurred and in compression where only twins dominated. A good agreement was obtained with the experiments. For polycrystalline Mg, they assumed a sigmoidal stress-strain response during the evolution of the twin volume fraction and achieved satisfactory agreements with experiments for both tension and compression. In another approach presented by Barnett et al. (2015), the appearance of avalanche-type interaction twins that nucleate from grain boundaries was considered. The effect of grain size on the twin volume fraction and on the yield strength could be modelled by their approach in deformed Mg alloys. Moreover, the general shape of the strain hardening curve up to ~0.15 compressive strain was reproduced.

All the previous models were either developed for TWIP steel for larger strain by modelling only one feature (Bouaziz and Guelton, 2001; Karaman et al., 2000) or were restricted to very small strains (Barnett et al., 2005) for Mg. The most complete model is by

Barnett et al. (2015), however, it still needs the twin volume fraction as an input for the polycrystal case.

It is well ascertained from the crystallographic point of view that there exist six extension twins, i.e. three paired extension twin variants, which may be activated during deformation of HCP polycrystals. The paired extension twins are at ~7.4° misorientation to each other (Nave and Barnett, 2004; Mu et al., 2014) and their occurrence within the same grain tends to consume the entire parent matrix (Mu et al., 2011). Molodov et al. (2014, 2016), Capolungo et al. (2009), and Beyerlein and Tomé (2010) showed the frequent existence of paired extension twin variants and also reported that extension twins with higher Schmid factor are most likely to be dominant by occupying a significant portion of the parent matrix or the whole matrix. At the same time, low Schmid factor extension twins represent only a negligible parent grain volume.

In the present work, a new analytical approach is established to address several features relevant to the twin induced deformation behaviour of polycrystalline metallic materials. This includes: (i) strain hardening behaviour, (ii) evolution of twin volume fraction and (iii) stress and strain partitioning between the matrix and the twins up to strain to failure. The model uses a simplified crystal plasticity hardening function (Kalidindi et al., 1992; Zhou et al., 1993) in which strain partitioning between the twin and matrix domains was incorporated with the help of the uniform energy composite approach (Bouaziz and Buessler (2002, 2004)). The novelty of this work is to accurately predict for the first time both the sigmoidal type flow curve and the twin volume fraction. The approach was validated by reproducing the experimental flow curves and the variations in twin volume fraction during quasi-static compression of the Mg-3Al-0.3Mn alloy measured in two sample orientations. Finally, the approach was also validated for the no twinning condition.

2. Modelling principles

2.1. Composite approach

The mechanics of the twinning activity in the present approach is based on a simple two-phase composite model in which one phase is the parent grain (also referred to as matrix) and the other is the twinned portion. The twinned part may contain multi-variant twins and is considered as a single phase. The present composite model uses the uniform plastic power approach, originally proposed by Bouaziz and Buessler (2002, 2004). Later, this approach was

successfully implemented in the works of Montheillet and Damamme (2005) and Toth et al. (2009). It is also called as the Iso-W model (Toth et al., 2009), and assumes that the plastic power is uniformly distributed within the composite, thus:

$$\dot{\varepsilon}\sigma = \dot{\varepsilon}_m\sigma_m = \dot{\varepsilon}_t\sigma_t \,. \tag{1}$$

The left-hand side of Eq. (1) is the macroscopic plastic power per unit volume, where σ is the macroscopic flow stress in compression and $\dot{\varepsilon}$ is the macroscopic compressive strain rate. The product is equal for both phases. The subscripts *m* and *t* stand for the matrix and the twin phases, respectively. $\dot{\varepsilon}_m$ and $\dot{\varepsilon}_t$ are the strain rates, σ_m and σ_t are the flow stresses. Concerning the strains in the individual phases, they produce the macroscopic strain according to the rule of mixture:

$$\varepsilon = f_m\varepsilon_m + f_t\varepsilon_t \,. \tag{2}$$

The time derivative of this equation is expressed as follows:

$$\dot{\varepsilon} = \dot{f}_m\varepsilon_m + f_m\dot{\varepsilon}_m + \dot{f}_t\varepsilon_t + f_t\dot{\varepsilon}_t \,. \tag{3}$$

Here, f_m and f_t are the volume fractions, which satisfy the following equation:

$$f_m + f_t = 1 \,. \tag{4}$$

2.2. Kinetics of the twinning activity

In order to establish the kinetics of the twinning activity for this analytical approach, some elements were considered from crystal plasticity. In crystal plasticity, an increment of the twin volume fraction is calculated from the twinning shear increment, $\Delta\gamma_t$, during a macroscopic strain increment, $\Delta\varepsilon$. The twinning systems are considered as pseudo-slips in a crystal plasticity code. From the twinning shear, the rate of growth of the twin can be determined using the following expression:

$$\dot{V}_t = V_m\frac{\dot{\gamma}_t}{\gamma_o}, \tag{5}$$

where V_t and V_m are the volumes of the twin and matrix phases, respectively, and γ_o is the twinning shear. The total slip rate $(\dot{\gamma}_r)$ within a grain is produced by slip $(\dot{\gamma}_s)$ and twinning pseudo-slip $(\dot{\gamma}_t)$:

$$\dot{\gamma}_r = \dot{\gamma}_s + \dot{\gamma}_t \ . \tag{6}$$

During the early stage of compression, the matrix does not change its crystallographic orientation significantly. As a result, the relative activities of the slip systems remain nearly constant within the mother grains. Henceforth, the total shear strain rate within the matrix can be expressed as:

$$\dot{\gamma}_r = A\dot{\gamma}_t \ . \tag{7}$$

Here *A* is a parameter ($A > 1$) which expresses the ratio of the total slip rate to the pseudo twin-slip within the mother grains. At the same time, the total slip rate in the matrix can be related to the macroscopic compression rate via the Taylor factor of the mother grain, M_m:

$$\dot{\gamma}_r = M_m \dot{\varepsilon} \ . \tag{8}$$

Combining Eqs. (7) and (8), the twinning shear strain rate can be expressed as:

$$\dot{\gamma}_t = \frac{M_m}{A}\dot{\varepsilon} \ . \tag{9}$$

Substituting the above expression into Eq. (5), the following can be obtained:

$$\dot{V}_t = V_m \frac{M_m}{A\gamma_o}\dot{\varepsilon} \ . \tag{10}$$

For simplification, all the constants; M_m, *A* and γ_o can be collectively denoted as *B*, thus:

$$\dot{V}_t = V_m B\dot{\varepsilon} \ , \text{ where } B = \frac{M_m}{A\gamma_o} \ . \tag{11}$$

The growth of the twin fraction within the parent grain is schematically illustrated in Fig. 1. From this figure, the evolution of the volume fractions for the twin and the matrix can be written as:

$$f_t = \frac{x}{a} \quad , \quad f_m = 1 - f_t \ . \tag{12a,b}$$

Eq. (11) can be written in incremental form to show that during a strain increment $d\varepsilon$, the twin volume increases by dV_t:

$$dV_t = V_m B\, d\varepsilon \ . \tag{13}$$

By using the geometry displayed in Fig. 1, the above equation can be expressed as:

$$bcdx = (a-x)bcBd\varepsilon \quad \Rightarrow \ dx = (a-x)Bd\varepsilon \tag{14}$$

Further, by integrating the above equation, the thickness of the twin phase can be obtained as a function of the compressive strain:

$$x = \frac{a\left(e^{B\varepsilon} - 1\right)}{e^{B\varepsilon}} . \tag{15}$$

Now using Eqs. (12a,b) and (15), the volume fractions of the matrix and twin phases can be expressed as a function of strain:

$$f_m = e^{-B\varepsilon} \quad , \quad f_t = 1 - e^{-B\varepsilon} . \tag{16a,b}$$

The time derivatives of the volume fractions are:

$$\dot{f}_m = -B\dot{\varepsilon}e^{-B\varepsilon}, \quad \dot{f}_t = B\dot{\varepsilon}e^{-B\varepsilon} . \tag{17a,b}$$

Now using Eqs. (1-4), the following relations can be obtained for the strain rates in the two phases:

$$\dot{\varepsilon}_t = \frac{\dot{\varepsilon} f_m - \varepsilon \dot{f}_m - \varepsilon_t \dot{f}_t}{f_m f_t + f_m f_m \sigma_t / \sigma_m} \quad , \quad \dot{\varepsilon}_m = \dot{\varepsilon}_t \frac{\sigma_t}{\sigma_m} . \tag{18a,b}$$

These differential equations cannot be solved in a closed form because the strain rates depend on the flow stresses of the phases, which evolve with strain. Nevertheless, they can be readily incremented numerically with small increments starting from zero plastic strain to obtain the strain accumulation in the matrix and twin phases.

2.3. Hardening law

For the evolution of the flow stress during plastic strain, we propose the following approach. A frequently used crystal plasticity hardening law established by Kalidindi et al. (1992) and further developed by Zhou et al. (1993) is considered here to model the strain hardening behaviour. By simplifying the self and latent hardening matrix in the original crystal plasticity hardening law, the following two equations can be established for each phase, indexed by *i*:

$$\dot{\sigma}_i = \mathrm{H}(\sigma)_i \, \dot{\varepsilon}_i \ , \tag{19}$$

$$\mathrm{H}(\sigma)_i = h_i \left(1 - \frac{\sigma}{\sigma_{sat}} \right)^n \ . \tag{20}$$

Here, $\mathrm{H}(\sigma)_i$ is a hardening function, h_i and n are the hardening parameters, and σ_{sat} is the saturation stress. Now incorporating the hardening function from Eq. (20) into Eq. (19), the increment of the flow stress can be expressed as:

$$d\sigma_i = h_i \left(1 - \frac{\sigma}{\sigma_{sat}} \right)^n d\varepsilon_i \ . \tag{21}$$

After separation of the variables and integrating Eq. (21), the following can be achieved:

$$\sigma_i = \sigma_{sat} - P^{\frac{1}{1-n}} \ , \tag{22a}$$

where $$P = \begin{cases} \dfrac{h_i (n-1)}{\sigma_{sat}^n} \varepsilon_i + \left(\sigma_{sat} - \sigma_0 \right)^{1-n} & \text{if} \quad \varepsilon_i \le \varepsilon_{i,sat} \ , \qquad (22b) \\ 0 & \text{if} \quad \varepsilon_i \ge \varepsilon_{i,sat} \ , \qquad (22c) \end{cases}$$

$$\text{with } \varepsilon_{i,sat} = \frac{\sigma_{sat}^{n}\left(\sigma_{sat}-\sigma_{0}\right)^{1-n}}{h_i\left(1-n\right)} \quad . \tag{22d}$$

In these equations $\varepsilon_{i,sat}$ is the strain value where the stress state reaches the saturation stress in the given phase, and σ_0 is the initial flow stress. Finally, the energy equation (Eq. 1) can be used to express the macroscopic flow stress of the composite:

$$\sigma = \frac{\dot{\varepsilon}_t}{\dot{\varepsilon}}\sigma_t \quad . \tag{23}$$

3. Experiments: materials, testing and characterization

Hot extruded Mg-3Al-0.3Mn alloy bar was tested under quasi-static conditions for both uniaxial compression and tension tests at ambient temperature until failure. The bar was in as-received state, without prior annealing. The specimens for compression had cuboidal geometry with square-shaped loading faces and height to width ratio of 3:2 as per ASTM E9-09 standard. Two types of compression tests were carried out: one with the compression direction (CD) parallel, and another where CD was perpendicular to the extrusion direction (ED) of the original bar. These specimens are designated here as CD∥ED and CD⊥ED, respectively. The geometry of the initial bar and the orientations of the two kind of samples are shown in Fig. 2 together with the main components of the crystallographic texture with the help of the hexagonal unit cell. The tests were performed on a computer controlled Instron 8800 Servo-Hydraulic machine at a constant nominal strain rate of $7.4\text{x}10^{-4}$ s^{-1}. Five samples were deformed for each orientation to ensure data reliability. For the compression tests, Teflon strips were used to reduce the friction between the sample surface and the compression platens. The tension tests were carried out on flat specimens along the extrusion direction with dimensions: 5 mm gage length, 20 mm total length and 0.5 mm thickness. The mechanical responses were acquired in terms of engineering stress-strain curves. Further, the obtained data were numerically computed to obtain the true stress-strain curve. The CD∥ED samples were deformed to true compression strains of 0.04, 0.08, 0.12 and 0.18, whereas the CD⊥ED samples were deformed to strains of 0.04, 0.08 and 0.12. The mentioned highest strain levels for both cases correspond to the point after which the samples fractured, while the tension tests were carried out until failure, up to a true tensile strain of 0.16.

The microstructures of the samples prior to and after deformation were characterized by the Electron Back Scattered Diffraction (EBSD) technique using a Field Emission Gun – Scanning Electron Microscope (FEG-SEM). In this regard, the specimens were sectioned at their centre on the plane with normal direction to the actual CD. Subsequently, the specimens were subjected to mechanical polishing with emery paper up to ~4 μm roughness, followed by chemical polishing using a solution of 75 mL ethane-diol, 24 mL distilled water and 1 mL HNO_3 over a polishing cloth to obtain a mirror finish. Finally, the residual stress surface layer was removed by electrolytic polishing in a solution of ethanol and ortho-phosphoric acid (volume fraction - 3:5) at ~0ºC, using a stainless-steel cathode at 3 V for 30 s and 1.5 V for 2 min (Biswas et al., 2010). The orientation mappings were performed using the HKL Channel 5 software. To ensure significant statistics, large areas containing well over 2500 grains were scanned. The acquired data were post-processed using the TSL and ATEX software (Beausir and Fundenberger, 2017).

4. Results

4.1. Strain hardening response

Fig. 3 displays the flow curves together with its true strain hardening rate $\left(d\sigma/d\varepsilon\right)$ obtained during quasi-static uniaxial compression for the two loading configurations (CD∥ED and CD⊥ED). It was found that the initial orientation had a pronounced effect on the flow curves. The offset yield strength was found to be ~72 MPa for CD∥ED and ~54 MPa for CD⊥ED. Correspondingly, the strain to failure was noted to be ~0.20 and ~0.13, respectively. The appearance of a sigmoidal shaped flow curve is the signature of twinning resulting in the concomitant increase in the strain hardening rate (Agnew et al., 2001; Dixit et al., 2015; Knezevic et al., 2010; Mu et al., 2011, 2014; Wang et al., 2012). Notably, this tendency was more pronounced in CD∥ED samples as compared to the CD⊥ED samples. The associated sigmoidal strain hardening curve can be characterized by three distinct regimes categorized as Stages I-II-III. Stage I is a regime of decreasing strain hardening rate followed by Stage II, where the strain hardening rate is increasing and finally Stage III, during which the strain hardening rate is decreasing with strain (Jiang et al., 2007; Mu et al., 2011, 2014; Salem et al., 2003).

4.2. Evolution of microstructure and crystallographic texture

Figs. 4 and 5 display the inverse pole figure map (IPF-map) for the as-received material, as well as for the compression tested samples for CD∥ED and CD⊥ED, respectively. In these maps, the colour key code represents the direction normal to the map in the crystal reference system of the grains. The corresponding crystallographic textures are presented in Figs. 6 and 7 in inverse pole figures of the actual compression axis (CD). For both testing conditions the as-received microstructures (Fig. 4a and Fig. 5a) are the same; only rotated by 90º with respect to the compression direction (CD). The microstructure of the as-received material exhibited an average grain size of ~108 μm. It mostly contained elongated grains along the extrusion direction with few small equiaxed grains. The microstructures initially were entirely devoid of twins. With increasing deformation, twins developed with lenticular shapes in green and blue colours in the IPF-maps representing nearly perpendicular orientations with respect to the actual CD direction.

4.2.1. Compression parallel to the extrusion direction

For the CD∥ED case (Fig. 4), the initial microstructure had only grains with c-axis aligned nearly perpendicular to CD. In order to show this explicitly, hcp unit cells were superimposed on the as-received IPF map in Fig. 4a. This was further substantiated with the aid of the IPF, displayed in Fig. 6a, that clearly characterizes the initial texture by a relatively strong intensity for $\langle 11\bar{2}0\rangle$∥CD (~8.6 MRD, multiples of random distribution) and a weak $\langle 10\bar{1}0\rangle$∥CD component (~2.4 MRD).

Upon deformation to a true compression strain of ~ 0.04, it can be observed that thin lenticular-shape morphology dominated in each grain for the entire microstructure (Fig. 4b). These morphological structures are identified as $\{10\bar{1}2\}\langle\bar{1}011\rangle$ type extension twins with ~86° misorientation about $\langle 11\bar{2}0\rangle$ with respect to the surrounding matrix. These twins appeared in the IPF of Fig. 6b around the $\langle 0002\rangle$ direction with an intensity of ~5.2 MRD, while the $\langle 11\bar{2}0\rangle$ component was weakened to ~6.7 MRD. This manifests that extension twin orients the grains such that their c-axis became almost parallel to CD. The fraction of twins in the microstructure was actually calculated based on this orientation difference of the matrix and the twins with respect to the CD axis. At the strain of 0.04, the fraction of twins present in the microstructure was ~0.39 ± 0.05. As the strain was increased to ~0.08, the twin fraction augmented to ~0.64 ± 0.04 (Fig. 3c). At $\varepsilon \approx 0.12$, the extension twins occupied the large portion of the

microstructure; ~0.79 ± 0.04 volume fraction (Fig. 4d). Finally, at $\varepsilon \approx 0.18$, almost ~0.93 ± 0.03 fraction of the microstructure was dominated by twin domains (Fig. 4e). The increase in the volume fraction of the extension twins with strain could be also verified by the gradual intensification of the $\langle 0002 \rangle$ component (~9.2 MRD) and diminishing of the $\langle 11\bar{2}0 \rangle$ component along CD in the IPFs of Figs. 6b-e. The large broadening of the extension twins by occupying the major portion of the microstructure is consistent with previous investigations (Molodov et al., 2014, 2016; Mu et al., 2011). The twin volume fractions as a function of the compression strain are plotted in Figs. 8b-c.

4.2.2. Compression perpendicular to the extrusion direction

For CD⊥ED, the initial microstructure is shown in Fig. 5a. Figs. 5 (a-i) and (a-ii) show a decomposition of the microstructure according to its two texture components; the $\langle 10\bar{1}0 \rangle$ and $\langle 0002 \rangle$, respectively, indicated by superimposed hcp cells. As can be seen in Fig. 5 (a-ii), a non-negligible fraction of matrix grains (~0.15) was already oriented near the CD direction, so they are not expected to twin. Figs. 5b-d show the evolution of the extension twins. The superimposed hcp cells indicate that the c-axes were almost parallel to CD before fracture (Fig. 5d). This is well displayed in the corresponding IPF (Fig. 7), where the intensity of the $\langle 0002 \rangle$ ||CD component increased from ~2.0 to ~9.71 MRD with strain. Fig. 5b shows that ~0.40 ± 0.04 fraction of the microstructure underwent twinning after $\varepsilon \approx 0.04$. As the strain increased further, from 0.08 to 0.12, the twin volume fraction changed from ~0.67 ± 0.04 to ~0.76 ± 0.03, see Fig. 8c.

4.3. Simulation results

The above presented experimental results were simulated with the help of the analytical approach described in Section 2, for both sample orientations. Several parameters were needed to be identified; see a detailed presentation of the parameter tuning process in Section 5 below. The approach can (i) describe the stress-strain curve, (ii) model the twin volume fraction evolution, and (iii) predict the partition between the twin and matrix phases for stress as well as strain. Fig. 3 shows the simulated stress-strain and strain hardening rate curves in comparison with the experimental ones. As can be seen, there is an excellent agreement between simulation and experiment, even for the derivatives of the stress-strain curves, for both

sample orientations. Only the very initial parts of the curves were not reproduced, for the reason that the elastic part of the deformation was not considered in the model. It is particularly compelling that even the maximum in the stress-strain curve is reproduced which is appearing in both experiments and in the simulation in Stage III, before fracture.

The prediction of the twin volume evolution is compared with the experiments in Figs. 8b and 8c. Again, excellent agreement can be observed. Actually, the twin volume fraction curves for the CD∥ED and CD⊥ED cases are identical. This is a consequence of the analytical formulas for the twin volume fractions given by Eqs. (16a-b), which contain only one parameter; the B. B is necessarily the same for both loading cases, because the experimental twin volumes were the same for both. The value of the B parameter was identified to be 13.92, see the variations of the predicted curves in Fig. 8a for different values of the B parameter, ranging from 0.05 to 20. Hence, the first parameter determined for the analytical model was B. Thereafter, the tuning of the hardening parameters could be accomplished.

The present analytical model predicts also the partition of stress and strain between the two phases; the matrix and the twins. The predicted results are displayed in Fig. 9 for both stress and strain. As expected, the twins harden more rapidly than the matrix, especially for the sample CD∥ED. Alternatively, the strain is less in the twins compared to the matrix strain, although not much less than the macroscopic imposed strain. The contrast is especially high for the CD∥ED case. The saturation stress could be reached in the twins for both sample orientations; at strains of 0.13 and 0.09, for the CD∥ED and CD⊥ED cases, respectively. The meaning of the obtained results will be discussed in Section 6, after presenting the procedure for obtaining the hardening parameters of the model.

5. Identification of the model parameters

As mentioned in the preceding section, the evolution of the twin volume fraction as a function of strain is only controlled by the B parameter. Fig. 8a was presented for showing the dependence of twinning activity on this parameter. So, it is straightforward to determine the appropriate B value, which was found to be 13.92 for both loading conditions. However, the analytical stress-strain relation (expressed by Eqs. 22-23) contains several other parameters which needs to be determined. (Note that Eqs. 22-23 depend also on the B value, through the strain partition relations of Eqs. 16-18.) The remaining parameters are: initial flow stress, σ_0, hardening coefficients, h_i, saturation stress, σ_{sat}, and the hardening exponent n appearing in

Eq. (23) for each domain. The subscript $i = m, t$ corresponds to the matrix and the twin phases, respectively. The total number of hardening parameters are five, taking into account that the same values were allocated for σ_0 , σ_{sat} and n for both the matrix and twin phases. This is a reasonable hypothesis, as both phases begin with the same material properties and during deformation only their crystallographic orientations were different.

The determination of the hardening parameter values was done using the following procedure:

a. Two parameters can be readily identified from the measured stress-strain curve: the yield stress, σ_0, and the saturation stress, σ_{sat}. The first is the flow stress at the onset of plastic deformation and the second is the maximum flow stress, which was also available, since the measured curve presented a maximum before fracture. The following values were found: 72 MPa and 54 MPa for σ_0, as well as 282 MPa and 222 MPa for σ_{sat} for the CD∥ED and CD⊥ED cases, respectively (see Fig. 3).
b. There remained three parameters to identify; the hardening coefficients h_m , h_t , and the n. They were identified by iteration, by looking for the best reproduction of the measured strain hardening curves. During the iteration process, the following characteristics were considered: higher hardening coefficient for the twin, so $h_t > h_m$, and $0 < n < 1$.
c. For a given set of assumed parameters, the stress-strain curves were constructed in the following way: First the plastic strains for both the matrix and the twin phases were set to zero. Then a simple loop started by incrementing the macroscopic true strain, $\mathcal{E}$. Within the loop, first the volume fraction of twins and their derivatives were calculated using Eqs. 16 and 17. Simultaneously, the strain increments were obtained from Eq. 18 and were accumulated in the phases (ε_m and ε_t). These strain values together with the hardening parameters were further used in Eq. 22a to obtain the flow stresses of the individual phases. Finally, Eq. 23 provided the macroscopic stress.

The identified values of all parameters are presented in Table 1 (they are also listed in the inset of the hardening curves in Fig. 3).

6. Discussion

In the present study, we introduced a new analytical approach for modelling strain hardening and twinning activity in a highly twinning Mg alloy. The model was applied for two

cases on the same material, by changing the orientation of the loading direction with respect to the initial texture. Strain hardening generally takes place due to two reasons: intrinsic hardening by accumulation of dislocations, and by geometrical hardening due to radical texture evolution induced by twinning. The analytical model captures both these characteristics at the same time but does not separate the contribution of the intrinsic and geometrical hardening. The purpose of the first part of the following discussion is to try to estimate separately the magnitude of the two hardening mechanisms. Then we examine the possible effect of Hall-Petch hardening caused by grain size variations. After that, the alloy behaviour will be examined by its composite nature, with the help of the simulated results on the stress and strain partitioning between the matrix and twin phases.

6.1. Textural hardening due to twin-induced reorientation of the crystallographic lattice

It is well ascertained that strain-hardening can take place by crystallographic reorientation of the matrix due to extension twinning, which orients the c-axis of the twinned domain nearly parallel to CD (Figs. 6 and 7) (Agnew et al., 2002; Knezevic et al., 2010; Mayama et al., 2011; Obara et al., 1973; Stohr and Poirier, 1972). Besides, the continuous increase in the harder oriented extension twin domains would require higher macroscopic stress for increasing plastic strain (Wang et al., 2012). In polycrystalline Mg alloys, it is expected that the stress required for twinning is low (Barnett et al., 2004) and the strain-hardening mechanisms are rather related to the stress needed to initiate slip within the twinned domain (Agnew et al., 2003). The hardening coefficients, h_m and h_t depend on the crystallographic texture; h_t is always higher, as it is dependent on the microstructure that contains mostly grains with c-axis ‖ to CD, i.e., harder orientations.

The effect of texture on hardening, i.e. the so-called geometrical hardening effect, can be examined with the help of the Taylor factor of the polycrystal, *M*. Here, the Taylor factor has been used only for discussion purposes, that is, for understanding and interpreting the obtained analytical modelling results. Note that the calculated Taylor factors were *not* used in our analytical modelling.

The general Taylor factor is defined for a grain as the sum of all crystallographic slip rates ($\dot{\gamma}_s$) divided by the macroscopic applied von-Mises equivalent strain rate ($\overline{\dot{\varepsilon}}$):

$$M = \sum_s \|\dot{\gamma}_s\| \Big/ \bar{\dot{\varepsilon}} \quad .$$

For a polycrystal, the individual *M* values are averaged over all orientations. This definition of the Taylor factor is valid also for several slip system families with different CRSS values when a proper definition for an average resolved shear stress is introduced; see Appendix.

The Taylor factors were computed using the VPSC polycrystal model of Molinari et al. (1987) and Molinari and Toth (1994) in its tangent approach formulation for the interaction between a given grain and the homogeneous equivalent medium. In VPSC polycrystal modelling, hard oriented grains deform less and softer grains deform more than the imposed macroscopic strain. In this way, the VPSC Taylor factor calculation is consistent with the results of the analytical modelling. Grains were identified from the EBSD maps (several thousand for each deformation state) and used in the VPSC code. For the calculation, the boundary condition corresponding to compression was imposed on the polycrystal in the direction parallel as well as perpendicular to ED. Basal, prismatic, pyramidal $\langle c + a \rangle$/I, pyramidal $\langle c + a \rangle$/II slip systems were considered to be available for both the matrix and twin domains. The critical resolved shear stress (CRSS) ratio in the same order was found to be 1:2:6:6, respectively. These CRSS values were obtained by matching the experimental flow curves as well as the texture evolution for the compression tests with the simulated ones (detailed results will be presented in a future publication). Similar CRSS values were also reported by Tang et al. (2014) and Lévesque et al. (2016).

By using the same CRSS ratios for the matrix and twin regions, only the effect of orientation is considered, that is, only geometrical hardening. The average *M* is displayed in Table 2 and the frequency distributions of the obtained *M* values are plotted in Fig. 10 as a function of strain.

It can be seen from Fig. 10 that the Taylor factor distribution is forming two peaks and moving towards higher values as strain increases. It must be noted that the presence of some, very small Taylor factors (less than 1.0) are due to the self-consistent approach in which individual grains can deform much less than the macroscopic strain. Initially, for the CD∥ED case, there is only one maximum, however, for CD⊥ED, there are two. This is a consequence of the difference in the initial textures between the two samples. For CD∥ED, all grains' c-axes are in nearly perpendicular orientation with respect to the compression direction, while for the

CD⊥ED sample, there is a second population of grains with c-axis parallel to the compression direction (see Figs. 2, 6 and 7). The latter matrix grains are in 'hard' orientations. They are actually in the orientation where the other matrix grain population will twin during deformation. The first peak is identified as 'Matrix' and the second as 'Twin' in Fig. 10. As expected, the twins have Taylor factors nearly twice higher than the matrix. The average *M* values increased somewhat less than that (see Table 2); they were only about 1.58 and 1.41 times, for the CD∥ED and CD⊥ED cases, respectively. At the same time, the experimental flow stress increased approximately by a factor of four for both samples (see Fig. 3). This indicates that the amount of strain hardening between the initial and final state cannot be explained solely by geometrical hardening. The difference must be caused by intrinsic hardening, due to dislocations, which is the subject of the next section.

6.2. Intrinsic hardening by dislocations

Dislocations are classified into two groups, according to the resultant burgers vector value that the dislocation group is producing. When a group has zero total burgers vector, the dislocations in the group are called statistically stored dislocations (SSDs). On the other hand, when a group of dislocations show a non-zero resultant burgers vector, the group contains the so-called geometrically necessary dislocations (GNDs). Naturally, statistical dislocations do not produce orientation differences, while GNDs do. Therefore, it can be expected, that by measuring the average grain orientation spread (GOS), one can relate it to the GND density. The GOS characterizes the average variance in the orientation of all scanned pixel within a grain with reference to the average orientation of the same grain (Wright et al., 2011). GOS can be readily obtained from EBSD measurements by first identifying the grains, then calculating GOS in each of them, finally, averaging over the whole population of grains. It is important to emphasize that GOS is due to lattice curvatures and geometrically necessary boundaries (GNBs), both are produced by GNDs. However, GOS is insensitive to the statistical dislocation density. Further, in order to use GOS for GND density considerations, it is necessary to consider the sizes of the grains. Therefore, the experimentally obtained GOS values were divided by the respective grain sizes (d) before the average GOS/d was calculated. The use of GOS/d for GND density considerations was introduced by Allain-Bonasso et al. (2012) and Wagner et al. (2011).

At lower strains, it was shown separately by Hughes (2001), Humphreys and Hatherly (2004), and Zhu et al. (2018) that both the GND and SSD density increases with strain. Hence, it is assumed that at lower strains, GOS/d is proportional to the total dislocation density. GOS/d was calculated separately for the matrix and twin domains with increasing strain and are plotted in Figs. 11a and 11b for the CD∥ED and CD⊥ED samples, respectively. As can be seen in Fig. 11, the average GOS/d values increase steadily with strain for both the matrix and the twins, by a factor of ~7x for CD∥ED and about 5x for CD⊥ED. Therefore, if we consider the assumed proportionality between GNDs and SSDs; the total dislocation density should have been increased by the same factor. That would involve an increase in the flow stress by the square-root of the dislocation densities, meaning an increase in the flow stress of $\sqrt{7} = 2.64\ x$, and $\sqrt{5} = 2.23\ x$, respectively. This increase in flow stress is to be added to the geometrical hardening ratio, which was 1.58 x and 1.41 x, respectively (see Section 6.1). The two hardening effects together should produce increases in the flow stress by $2.64\ x + 1.58\ x = 4.22\ x$ and $2.23\ x + 1.41\ x = 3.64\ x$, respectively. These values are actually not far from the increase in the experimental flow stress, which were 3.92 and 4.11. This analysis permits to conclude that the intrinsic hardening by dislocations contributed more to the strain hardening than the geometrical one (nearly twice more).

It is also clear that the GOS/d values are systematically higher for the matrix than for the twins, see Fig. 11. Consequently, the GND density must have been higher in the matrix phase. Since the GND density is obviously increasing with strain, this result is also in concordance with the model prediction, as larger strains were obtained for the matrix (Fig. 9).

6.3. Hall-Petch effect

It was observed in the present experiments that the development of extension twins at the very early deformation ($\varepsilon \approx 0.04$) led to an abrupt decrease in the average grain size: from ~108 μm to 38.5 μm and 55.6 μm for the CD∥ED and CD⊥ED cases, respectively (see Figs. 3 and 4). However, with further deformation, these extension twins broadened through migration of twin boundaries leading to an increase in the average grain size to ~73.5 μm for CD∥ED and ~86.4 μm for CD⊥ED at higher strains, see Fig. 3c-e and Fig. 4c-d, respectively. Therefore, hardening due to the decrease in the mean free path of dislocations i.e., due to grain size reduction can be ruled out. The broadening of twins and the consumption of matrix was earlier reported by Dudamell et al. (2011) during deformation of Mg alloy AZ31 at very high strain

rates. This is consistent with our findings and corroborates well with independent theoretical investigations performed by Knezevic et al. (2010) and Molodov et al. (2017). They showed that minimal Hall-Petch hardening occurs in Mg alloys because the extension twin domains broaden to consume the entire microstructure without introducing appreciable barrier effect to slip transmission across twin boundaries. Using molecular dynamic simulations, El Kadiri et al. (2015) have shown that extension twin boundaries absorb the basal dislocations as efficient sinks and thereby broaden the extension twin domain in Mg. Chichili et al. (1998) have shown no effect on flow stress in commercially pure Ti by the presence of deformation twins, substantiating our observation. On the contrary, Mahajan et al. (1973) and Gray et al. (1997) reported that the increase in strain hardening rate in Stage-II may occur due to the effective reduction in grain size in face-centred cubic (fcc) polycrystals and hcp (Ti) structures.

6.4. The composite behaviour

The stress and strain partition between the matrix and twin phases were presented in Fig. 9. Our analytical model predicts that the twin phase hardens more, and by the virtue of duality, the strain is less in the twin phase with respect to the matrix. The behaviour of the composite can be better analysed if we also look at the *strain rate* partition between the two phases as a function of strain; it is presented in Fig. 12. Comparing the strain rate variations in the matrix and the twins, one can observe that they are different. While the strain rate remains always smaller than the macroscopic one in the twin, at strains of 0.123 (CD∥ED) and 0.082 (CD⊥ED), the twin strain *rate* becomes the same and then slightly overshoots the macroscopic strain *rate*. The above critical strain values are given by Eq. 22d. Above this critical strain, the flow stress in the twin phase remains constant and equal to the saturation stress. By differentiating Eq. 1, we obtain the following differential relation for $\varepsilon > \varepsilon_{t,sat}$:

$$\dot{\sigma} = \frac{\dot{\dot{\varepsilon}}_t}{\dot{\varepsilon}} \sigma_{sat}, \quad \varepsilon > \varepsilon_{t,sat}. \tag{24}$$

This equation shows that after the critical strain, the macroscopic stress variation depends only on the second derivative of the twin-strain. As can be seen from Fig. 12, for $\varepsilon > \varepsilon_{t,sat}$ the derivative of the $\dot{\varepsilon}_t$ curve is first positive, then zero, then it becomes negative. Consequently, a maximum value of the flow stress is predicted for the composite when $\dot{\dot{\varepsilon}}_t = 0$. The predicted

strain values at the position of maximum flow stress are about 0.16 and 0.13, for the CD∥ED and CD⊥ED cases, respectively, in good agreement with the experiments (see in Fig. 3).

It is fascinating that this analytical model is able to predict the existence of a maximum value in the stress-strain curve of the composite, and in agreement with the experiments. Therefore, the observed maximum in the measurement has a physical reason which could be modelled. This is an important result of the present modelling. After the maximum, the stress has to decrease according to our equations. It is well known in mechanics that, when strain hardening becomes negative, the stability of the deformation is lost, and the deformation localizes in a macroscopic band in the sample leading to fracture. Thus, our analytical approach captures the onset of deformation instability.

6.5. Assessing for no-twinning condition

Another aspect that requires focus is to demonstrate the capability of the analytical model for the no-twinning condition. Recently, Qiao et. al (2015, 2017) demonstrated that a EVPSC - Twinning-DeTwinning (TDT) model could accurately predict the mechanical response attributed to large, intermediate and insignificant twinning conditions. The latter aspect is considered to be important for a model to be complete. In order to verify the predictive capacity of the present model for that case, the tensile test carried out parallel to the extrusion direction was also modelled. The initial microstructure for the tension is the same as shown in Fig. 4a. In this case, the grains had their c-axis perpendicular to the tension direction, a condition where twinning activity is negligibly small.

Under such circumstances, the *B*-parameter was identified to be 0.05 leading to only 0.01 twinning volume fraction. Fig. 13b displays the evolution of the volume fraction of the parent matrix and the twins as a function of true tensile strain. After defining the *B*-parameter, the other model parameters (σ_0, σ_{sat}, h_i and n) were identified following a similar procedure as discussed in Section 5. Figs. 13c,d show the simulated flow curve and the strain hardening rate plot using σ_0 = 142 MPa, σ_{sat} = 229 MPa, h_m = 2400 MPa, and n = 0.56. The predicted plots were in good agreement with the experimental ones for any value of the hardening coefficient assigned to the twin phase (h_t values ranging from 10 to 8000 MPa); the curves are practically coinciding. This is actually expected due to the very low volume fraction of the twins. Thus,

the new analytical model is capable to reproduce the mechanical response ranging from twinning dominance to non-twinning conditions appropriately.

7. Summary and Conclusion

A new analytical model is presented in this paper which can accurately predict the strain-hardening behaviour, the evolution of the twin volume fraction, and the partition of stress and strain between the matrix and twin phases in polycrystalline hcp materials where twinning is a relevant deformation mechanism. The predictive capability of the model was assessed by compression tests, carried out parallel and perpendicular to the axis of an extruded rod magnesium alloy Mg-3Al-0.3Mn during ambient temperature deformation. The model is composed of three basic elements: (i) A composite model with two phases; matrix and twin, in which the stress and strain partitioning is governed by the "Iso-work" hypothesis, (ii) A twinning kinetic equation, based on crystal plasticity elements, containing only one parameter (B), (iii) A strain hardening approach, which is a simplified version of the Kalidindi-type hardening law, originally used in crystal plasticity. It contains three parameters for each phase. The parameters of the model were identified by matching the predictions with the experimental results. In this process, the B parameter was identified first, and was found to be independent of the loading direction and also of strain hardening; rather it depends only on the material. It is, however, a relevant parameter in reproducing the shape of the strain hardening curve which is typically S-shaped. The strain hardening parameters were identified by matching the predicted strain hardening curve with the experimental one. Among the three parameters for each phase, only one was different: the hardening coefficient parameter, which was found to be higher for the twin phase.

The analysis of the obtained results permits us to conclude on the following main findings:

1. The applicability of the proposed analytical approach is verified for the present Mg-3Al-0.3Mn alloy. It is proved to be predictive with high precision for the stress-strain curve, and the twinning volume fraction.
2. The model predicts a maxima on the stress-strain curve which appears also in the experiment just before fracture.
3. Much higher strain hardening rate is predicted for the twins than for the matrix. With the help of a GOS/d analysis of the microstructures and using the Taylor factors, the higher

strength of the twin phase was due to both an orientation effect of the twins (textural hardening) and also due to intrinsic dislocation hardening.

Appendix

The Taylor factor for multiple CRSS values

Here we consider a crystal in which several slip system families can be activated at the same time with different CRSS values. The number of families is N and in a given family there is n_f number of slip systems. The Taylor factor is used to estimate the resistance of a grain with respect to a given loading. Its definition is based on the principle of work conjugacy:

$$\sum_{f=1}^{N}\sum_{s=1}^{n_f}\tau_s^f\dot{\gamma}_s^f=\sigma_{kl}\dot{\varepsilon}_{kl} \quad . \tag{A1}$$

Here the left side is the 'internal' and the right side is the 'external' plastic power. The internal power is the sum of the powers made by the individual slip systems: $\tau_s^f\dot{\gamma}_s^f$. The external one is calculated by the multiplication of the applied stress tensor and the macroscopic strain rate tensor: $\sigma_{kl}\dot{\varepsilon}_{kl}$. The latter can be calculated also by their scalar equivalent quantities, so Eq. (A1) can be written as:

$$\sum_{f=1}^{N}\sum_{s=1}^{n_f}\tau_s^f\dot{\gamma}_s^f=\bar{\sigma}\cdot\dot{\bar{\varepsilon}} \quad . \tag{A2}$$

Here $\dot{\bar{\varepsilon}}$ can be chosen as the von-Mises equivalent strain rate, while $\bar{\sigma}$ is not the von Mises equivalent stress (because a crystal is not a von Mises material), it is just called equivalent stress ($\bar{\sigma}$ is actually defined by Eq. (A2)).

The τ_s^f quantity is the resolved shear stress, which is calculated by the projection of the stress state on the given slip system, the system being represented by the Schmid orientation matrix $m_{s,ij}^f$:

$$\tau_s^f=\sigma_{ij}m_{s,ij}^f \quad . \tag{A3}$$

τ_s^f is the same as the CRSS in rate insensitive slip while it is related to the slip rate in viscoplastic slip. Here we consider both cases.

For the case of multiple slip families, we first define an *average resolved shear stress* $\bar{\tau}$ using the slip rates:

$$\bar{\tau} = \sum_{f=1}^{N}\sum_{s=1}^{n_f} \tau_s^f \dot{\gamma}_s^f \Big/ \sum_{f=1}^{N}\sum_{s=1}^{n_f} \left\| \dot{\gamma}_s^f \right\| \quad . \tag{A4}$$

In this equation the denominator is simply the total slip rate. With the help of the average resolved shear stress, Eq. (A2) can be rewritten as:

$$\bar{\tau}\sum_{f=1}^{N}\sum_{s=1}^{n_f} \left\| \dot{\gamma}_s^f \right\| = \bar{\sigma} \cdot \bar{\dot{\varepsilon}} \quad . \tag{A5}$$

This equation defines the Taylor factor in two expressions; one with the slips, the other with the equivalent stresses:

$$M = \frac{\sum_{f=1}^{N}\sum_{s=1}^{n_f} \left\| \dot{\gamma}_s^f \right\|}{\bar{\dot{\varepsilon}}} = \frac{\bar{\sigma}}{\bar{\tau}} \quad . \tag{A6}$$

In a crystal plasticity simulation, the ratio of the total slip rate to the equivalent strain rate is available, and defines the general Taylor factor. Eq. (A6) shows it is also equal to the ratio of the external equivalent stress and the average resolved shear stress, which represents the 'resistance' or 'strength' of the crystal with respect to the loading. While the CRSS values do not appear directly in the formula for the Taylor factor, they are the parameters to be used in the crystal plasticity solution.

Acknowledgements

The authors acknowledge the financial support provided by the Science and Engineering Research Board (Ref. no.: ECR/2016/000125), Department of Science and Technology, Government of India. The work was also supported by the National Research Agency, France

referenced as ANR-11-LABX-008-01 (LabEx DAMAS). The work also used the facility 'Light Metals and Alloys Research Lab' setup at Department of Metallurgical and Materials Engineering, Indian Institute of Technology, Kharagpur, India.

References

Agnew, S.R., Horton, J.A., Yoo, M.H., 2002. Transmission electron microscopy investigation of ⟨c + a⟩ dislocations in Mg and α-solid solution Mg-Li alloys. Metall. Mater. Trans. A 33 (13), 851-858.

Agnew, S.R., Tomé, C.N., Brown, D.W., Holden, T.M., Vogel, S.C., 2003. Study of slip mechanisms in a magnesium alloy by neutron diffraction and modeling. Scr. Mater. 48 (8), 1003-1008.

Agnew, S.R., Yoo, M.H., Tomé, C.N., 2001. Application of texture simulation to understanding mechanical behavior of Mg and solid solution alloys containing Li or Y. Acta Mater. 49, 4277-4289.

Allain-Bonasso, N., Wagner, F., Berbenni, S., Field, D.P., 2012. A study of the heterogeneity of plastic deformation in IF steel by EBSD. Mater. Sci. Eng. A 548, 56–63.

Allen, R.M., Toth, L.S., Oppedal A.L., El Kadiri, H., 2018. Crystal Plasticity Modeling of Anisotropic Hardening and Texture Due to Dislocation Transmutation in Twinning. Materials 11, 1855.

Ando, D., Koike, J., Sutou, Y., 2014. The role of deformation twinning in the fracture behaviour and mechanism of basal textured magnesium alloys. Mater. Sci. Eng. A 600, 145-152.

Ardeljan, M., Beyerlein, I.J., McWilliams, B.A., Knezevic, M., 2016. Strain rate and temperature sensitive multi-level crystal plasticity model for large plastic deformation behavior: Application to AZ31 magnesium alloy. Int. J. Plast. 83, 90-109.

ASTM E9-09, 2018. Standard test methods of compression testing of metallic materials at room temperature, ASTM International, West Conshohocken, PA, www.astm.org.

Barnett, M.R., Bouaziz, O., Toth, L.S., 2015. A microstructure based analytical model for tensile twinning in a rod textured Mg alloy. Int. J. Plast. 72, 151-167.

Barnett, M.R., Davies, C.H.J., Ma, X., 2005. An analytical constitutive law for twinning dominated flow in magnesium. Scr. Mater. 52 (7), 627-632.

Barnett, M.R., Keshavarz, Z., Beer, A.G., Atwell, D., 2004. Influence of grain size on the compressive deformation of wrought Mg-3Al-1Zn. Acta Mater. 52 (17), 5093-5103.

Basinski, Z.S., Szczerba, M.S., Niewczas, M., Embury, J.D., Basinski, S.J., 1997. The transformation of slip dislocations during twinning of copper-aluminum alloy crystals. Revue de Métallurgie 94 (9), 1037-1044.

Beausir, B., Biswas, S., Kim, D.I., Tóth, L.S., Suwas, S., 2009. Analysis of microstructure and texture evolution in pure magnesium during symmetric and asymmetric rolling. Acta Mater. 57 (17), 5061-5077.

Beausir, B., Fundenberger, J.J., 2017. Analysis tools for electron and X-ray diffraction, ATEX - software, www.atex-software.eu, Université de Lorraine - Metz.

Beyerlein, I.J., Tomé, C.N., 2010. A probabilistic twin nucleation model for HCP polycrystalline metals. Proc. Roy. Soc. A. 466 (2121), 2517-2544.

Biswas, S., Beausir, B., Toth, L.S., Suwas, S., 2013. Evolution of texture and microstructure during hot torsion of a magnesium alloy. Acta Mater. 61 (14), 5263-5277.

Biswas, S., Singh Dhinwal, S., Suwas, S., 2010. Room-temperature equal channel angular extrusion of pure magnesium. Acta Mater. 58 (9), 3247-3261.

Biswas, S., Sket, F., Chiumenti, M., Gutiérrez-Urrutia, I., Molina-Aldareguía, J. M., Pérez-Prado, M.T., 2013. Relationship Between the 3D Porosity and β-Phase Distributions and the Mechanical Properties of a High Pressure Die Cast AZ91 Mg Alloy. Metall. Mater. Trans. A 44 (9), 4391-4403.

Bouaziz, O., Buessler, P., 2002. Mechanical behaviour of multiphase materials: an intermediate mixture law without fitting parameter. Revue de Métallurgie 99 (1), 71-77.

Bouaziz, O., Buessler, P., 2004. Iso-work increment assumption for heterogeneous material behaviour modelling. Adv. Eng. Mater. 6 (12), 79-83.

Bouaziz, O., Guelton, N., 2001. Modelling of TWIP effect on work-hardening. Mater. Sci. Eng. A 319-321, 246-249.

Cáceres, C.H., Lukáč, P., Blake, A., 2008. Strain hardening due to $\{10\bar{1}2\}$ twinning in pure magnesium. Philos. Mag. 88 (7), 991-1003.

Capolungo, L., Beyerlein, I.J., Tomé, C.N., 2009. Slip-assisted twin growth in hexagonal close-packed metals. Scr. Mater. 60 (1), 32-35.

Chichili, D.R., Ramesh, K.T., Hemker, K.J., 1998. The high-strain-rate response of alpha-titanium: experiments, deformation mechanisms and modeling. Acta Mater. 46 (3), 1025-1043.

Christian, J.W., Mahajan, S., 1995. Deformation twinning. Prog. Mater. Sci. 39, 1-157.

Clausen, B., Tomé, C.N., Brown, D.W., Agnew, S.R., 2008. Reorientation and stress relaxation due to twinning: Modeling and experimental characterization for Mg. Acta Mater. 56 (11), 2456-2468.

Dixit, N., Xie, K.Y., Hemker, K.J., Ramesh, K.T., 2015. Microstructural evolution of pure magnesium under high strain rate loading. Acta Mater. 87, 56-67.

Dudamell, N.V., Ulacia, I., Gálvez, F., Yi, S., Bohlen, J., Letzig, D., Hurtado, I., Pérez-Prado, M.T., 2011. Twinning and grain subdivision during dynamic deformation of a Mg AZ31 sheet alloy at room temperature. Acta Mater. 59 (18), 6949-6962.

El Kadiri, H., Barrett, C.D., Wang, J., Tomé, C.N., 2015. Why are twins profuse in magnesium? Acta Mater. 85, 354-361.

Fernández, A., Pérez Prado, M.T., Wei, Y., Jérusalem, A., 2011. Continuum modeling of the response of a Mg alloy AZ31 rolled sheet during uniaxial deformation. Int. J. Plast. 27 (11), 1739-1757.

Fullman, R.L., 1953. Measurement of particle sizes in opaque bodies. JOM 5 (3), 447–452.

Graff, S., Brocks, W., Steglich, D., 2007. Yielding of magnesium: From single crystal to polycrystalline aggregates. Int. J. Plast. 23 (12), 1957-1978.

Gray, G.T., 1997. Influence of strain rate and temperature on the structure. Property Behavior of High-Purity Titanium. J. de Physique IV 07 (C3), 423-428.

Gu, C.F., Tóth, L.S., Field, D.P., Fundenberger, J.J., Zhang, Y.D., 2013. Room temperature equal-channel angular pressing of a magnesium alloy. Acta Mater. 61 (8), 3027-3036.

Guo, X.Q., Chapuis, A., Wu, P.D., Agnew, S.R., 2015. On twinning and anisotropy in rolled Mg alloy AZ31 under uniaxial compression. Int. J. Solids Struct. 64-65, 42–50.

Hu, Y., Randle, V., 2007. An electron backscatter diffraction analysis of misorientation distributions in titanium alloys. Scr. Mater. 56 (12), 1051-1054.

Hughes, D., 2001. Microstructure evolution, slip patterns and flow stress. Mater. Sci. Eng. A 319-321, 46-54.

Humphreys, F.J., Hatherly, M., 2004. Recrystallization and related annealing phenomena. UK: Elsevier.

Jahedi, M., McWilliams, B.A., Moy, P., Knezevic, M., 2017. Deformation twinning in rolled WE43-T5 rare earth magnesium alloy: Influence on strain hardening and texture evolution. Acta Mater. 131, 221-232.

Jain, A., Agnew, S.R., 2007. Modeling the temperature dependent effect of twinning on the behaviour of magnesium alloy AZ31B sheet. Mater. Sci. Eng. A 462, 29-36.

Jiang, L., Jonas, J.J., Luo, A.A., Sachdev, A.K., Godet, S., 2007. Influence of {10-12} extension twinning on the flow behavior of AZ31 Mg alloy. Mater. Sci. Eng. A 445-446, 302-309.

Jiang, L., Jonas, J.J., Mishra, R.K., Luo, A.A., Sachdev, A.K., Godet, S., 2007. Twinning and texture development in two Mg alloys subjected to loading along three different strain paths. Acta Mater. 55 (11), 3899-3910.

Joost, W.J., Krajewski, P.E., 2017. Towards magnesium alloys for high-volume automotive applications. Scr. Mater. 128, 107-112.

Kalidindi, S.R., Bronkhorst, C.A., Anand, L., 1992. Crystallographic texture evolution in bulk deformation processing of FCC metals. J. Mech. Phys. Solids 40 (3), 537-569.

Karaman, I., Sehitoglu, H., Beaudoin, A.J., Chumlyakov, Y.I., Maier, H.J., Tomé, C.N., 2000. Modeling the deformation behavior of Hadfield steel single and polycrystals due to twinning and slip. Acta Mater. 48 (9), 2031-2047.

Khan, A.S., Pandey, A., Gnäupel-Herold, T., Mishra, R.K., 2011. Mechanical response and texture evolution of AZ31 alloy at large strains for different strain rates and temperatures. Int. J. Plast. 27 (5), 688-706.

Knezevic, M., Capolungo, L., Tomé, C.N., Lebensohn, R.A., Alexander, D.J., Mihaila, B., McCabe, R.J., 2012. Anisotropic stress–strain response and microstructure evolution of textured α-uranium. Acta Mater. 60 (2), 702-715.

Knezevic, M., Levinson, A., Harris, R., Mishra, R.K., Doherty, R.D., Kalidindi, S.R., 2010. Deformation twinning in AZ31: Influence on strain hardening and texture evolution. Acta Mater. 58 (19), 6230-6242.

Knezevic, M., Zecevic, M., Beyerlein, I.J., Bingert, J.F., McCabe, R.J., 2015. Strain rate and temperature effects on the selection of primary and secondary slip and twinning systems in HCP Zr. Acta Mater. 88, 55-73.

Lay, S., Ayed, P., Nouet, G., 1992. A study of $(0\bar{1}12)$ twin deviating from exact orientation in magnesium. Acta Metall. Mater. 40 (9), 2351-2359.

Lévesque, J., Mohammadi, M., Mishra, R. K., Inal, K., 2016. An extended Taylor model to simulate localized deformation phenomena in magnesium alloys. Int. J. Plast. 78, 203-222.

Levinson, A., Mishra, R. K., Doherty, R. D., Kalidindi, S. R., 2013. Influence of deformation twinning on static annealing of AZ31 Mg alloy. Acta Mater. 61 (16), 5966-5978.

Lou, X.Y., Li, M., Boger, R.K., Agnew, S.R., Wagoner, R.H., 2007. Hardening evolution of AZ31B Mg sheet. Int. J. Plast. 23, 44-86.

Mahajan, S., Chin, G.Y., 1973. Twin-slip, twin-twin and slip-twin interactions in Co-8 wt.% Fe alloy single crystals. Acta Metall. 21 (2), 173-179.

Mayama, T., Noda, M., Chiba, R., Kuroda, M., 2011. Crystal plasticity analysis of texture development in magnesium alloy during extrusion. Int. J. Plast. 27 (12), 1916-1935.

Molinari A., Canova G.R., Ahzi S., 1987. A self consistent approach of the large deformation polycrystal plasticity. Acta metall. 35, 2983-2994.

Molinari A., Toth L.S., 1994. Tuning a self consistent viscoplastic model by finite element results – I. Modeling. Acta metal. Mater. 42 (7), 2453-2458.

Molodov, K.D., Al-Samman, T., Molodov, D.A., 2017. Profuse slip transmission across twin boundaries in magnesium. Acta Mater. 124, 397-409.

Molodov, K.D., Al-Samman, T., Molodov, D.A., Gottstein, G., 2014. Mechanisms of exceptional ductility of magnesium single crystal during deformation at room temperature: Multiple twinning and dynamic recrystallization. Acta Mater. 76, 314-330.

Molodov, K.D., Al-Samman, T., Molodov, D.A., Gottstein, G., 2016. On the role of anomalous twinning in the plasticity of magnesium. Acta Mater. 103, 711-723.

Montheillet, F., Damamme, G., 2005. Simple flow rules for modeling the behaviour of inhomogeneous viscoplastic materials. Adv. Eng. Mater. 7 (9), 852-858.

Mu, S., Al-Samman, T., Mohles, V., Gottstein, G., 2011. Cluster type grain interaction model including twinning for texture prediction: Application to magnesium alloys. Acta Mater. 59 (18), 6938-6948.

Mu, S., Tang, F., Gottstein, G., 2014. A cluster-type grain interaction deformation texture model accounting for twinning-induced texture and strain-hardening evolution: Application to Magnesium alloys. Acta Mater. 68, 310-324.

Nave, M.D., Barnett, M.R., 2004. Microstructures and textures of pure magnesium deformed in plane-strain compression. Scr. Mater. 51 (9), 881-885.

Niewczas, M., 2010. Lattice correspondence during twinning in hexagonal close-packed crystals. Acta Mater. 58 (17), 5848-5857.

Obara, T., Yoshinga, H., Morozumi, S., 1973. $\{11\bar{2}2\}\langle 1123\rangle$ Slip system in magnesium. Acta Metall. 21 (7), 845-853.

Proust, G., Tomé, C.N., Jain, A., Agnew, S.R., 2009. Modeling the effect of twinning and detwinning during strain-path changes of magnesium alloy AZ31. Int. J. Plast. 25 (5), 861-880.

Qiao, H., Agnew, S. R., Wu, P. D., 2015. Modeling twinning and detwinning behavior of Mg alloy ZK60A during monotonic and cyclic loading. Int. J. Plast. 65 , 61-84.

Qiao, H., Guo, X. Q., Oppedal, A. L., El Kadiri, H., Wu, P. D., Agnew, S. R., 2017. Twin-induced hardening in extruded Mg alloy AM30. Mater. Sci. Eng. A 687, 17-27.

Salem, A.A., Kalidindi, S.R., Doherty, R.D., 2003. Strain hardening of Titanium: role of deformation twinning. Acta Mater. 51 (14), 4225-4237.

Stohr, J.F., Poirier, J.P., 1972. Electron microscope study of Pyramidal Slip {1122}〈1123〉 in Magnesium. Philos. Mag. 25, 1313-1329.

Tang, W., Li, D., Huang, S., Zhang, S., Peng, Y., 2014. Simulation of texture evolution in magnesium alloy: Comparisons of different polycrystal plasticity modeling approaches. Computers & Structures 143, 1-8.

Tóth, L.S., Molinari, A., Bouaziz, O., 2009. Effective strain rate sensitivity of two phase materials. Mater. Sci. Eng. A 524 (1-2), 186-192.

Wagner, F., Allain-Bonasso, N., Berbenni, S., Field, D.P., 2011. On the use of EBSD to study the heterogeneity of plastic deformation. Mater. Sci. Forum 702-703, 245–252.

Wang, F., Agnew, S.R., 2016. Dislocation transmutation by tension twinning in magnesium alloy AZ31. Int. J. Plast. 81, 63-86.

Wang, B., Xin, R., Huang, G., Liu, Q., 2012. Effect of crystal orientation on the mechanical properties and strain hardening behavior of magnesium alloy AZ31 during uniaxial compression. Mater. Sci. Eng. A 534, 588–593.

Wright, S.I., Nowell, M.M., Field, D.P., 2011. A review of strain analysis using electron backscatter diffraction. Microscopy and Microanalysis 17 (03), 316-329.

Yoo, M.H., 1981. Slip, twinning and fracture in hexagonal close-packed metals. Metall. Mater. Trans. A 12 (3), 409-418.

Zhang, J., Joshi, S.P., 2012. Phenomenological crystal plasticity modeling and detailed micromechanical investigations of pure magnesium. J. Mech. Phy. Solids 60 (5), 945-972.

Zhou, Y., Neale, K.W., Tóth, L.S., 1993. A modified model for simulating latent hardening during the plastic deformation of rate-dependent FCC polycrystals. Int. J. Plast. 9 (8), 961-978.

Zhu, C., Harrington, T., Gray, G.T., Vecchio, K.S., 2018. Dislocation-type evolution in quasi-statically compressed polycrystalline nickel. Acta Mater. 155, 104-116.

Zilahi, Gy., 2018. Three-dimensional line profile analysis, PhD Thesis, Eotvos University, Budapest, Hungary.

Table captions:

Table 1. The identified parameter values for the analytical model for the two sample orientations in compression.

Table 2. The average Taylor factors obtained in axisymmetric compression for the IPF maps as a function of strain.

Figure Captions:

Fig. 1. Schematic representation of the matrix and twin phases in a grain showing the growth of a twin.

Fig. 2. Sample geometry and testing directions showing the extruded bar from where the samples were machined for CD∥ED marked as I and CD⊥ED marked as II. The hexagonal unit cell shows the orientation of the main texture components.

Fig. 3. Experimental and predicted flow curves and strain hardening rate plots of Mg-3Al-0.3Mn alloy during uniaxial compression test carried out (a) parallel and (b) perpendicular to the extrusion direction of the original bar.

Fig. 4. Measured inverse pole figure (IPF) maps of the Mg-3Al-0.3Mn alloy with compression direction parallel to the extrusion direction. (a) as-received extruded material, and deformed samples to strains of: (b) 0.04, (c) 0.08, (d) 0.12 and (e) 0.18. The hcp unit cells are superimposed on the initial and final states. The colour key code represents the direction normal to the map in the crystal reference system of the grains.

Fig. 5. IPF maps of Mg-3Al-0.3Mn alloy measured after compression perpendicular to the original extrusion direction. (a)-(a-i)-(a-ii): as-received extruded material showing the full microstructure in (a) and its partitioned microstructures in (a-i)-(a-ii). (a-i) shows grains with c-axis near perpendicular to CD while (a-ii) displays grains with c-axis parallel to CD. The deformed states are shown as a function of strain for (b) $\varepsilon = 0.04$, (c) $\varepsilon = 0.08$ and (d) $\varepsilon = 0.12$. Some hcp unit cells are superimposed in (a-i), (a-ii) and (d) for showing the characteristic orientations of the grains. The colour key code represents the direction normal to the map in the crystal reference system of the grains.

Fig. 6. Inverse pole figures of the CD axis in Mg-3Al-0.3Mn alloy for loading CD∥ED. (a) as-received, and compression tested samples up to intermediate strains of (b) 0.04, (c) 0.08, (d) 0.12 and (e) 0.18. The colour bar represents the multiples of random distribution (MRD).

Fig. 7. Inverse pole figures of the CD axis in Mg-3Al-0.3Mn alloy for loading CD⊥ED. (a) as-received, and compression tested samples up to intermediate strains of (b) 0.04, (c) 0.08 and (d) 0.12. The colour bar represents the multiples of random distribution (MRD).

Fig. 8. (a) Calibration of the B parameter for predicting the twin-volume fraction in Mg-3Al-0.3Mn alloy as a function of compression strain. The open circle markers represent the experimental twin volume fractions for the CD∥ED case. B = 13.92 was identified for both the (b) CD∥ED and (c) CD⊥ED loadings.

Fig. 9. Predicted variations of the stresses and strains for the matrix and the twin phases as a function of true compression strain for (a) CD∥ED and (b) CD⊥ED. The red dotted line represents the macroscopically imposed strain.

Fig. 10. Taylor factor distribution plots for the initial as well as for the deformed samples for (a) CD∥ED and (b) CD⊥ED.

Fig. 11. Average Grain Orientation Spread (GOS) divided by the grain diameters (d) obtained from the experimental microstructures for the initial and deformed samples of the Mg-3Al-0.3Mn alloy for the (a) CD∥ED and (b) CD⊥ED cases.

Fig. 12. Predicted strain rate partitions in the matrix and the twin phases as a function of strain for (a) CD∥ED and (b) CD⊥ED. Horizontal dashed line represents the macroscopic strain rate and the vertical dashed line represents the position where the twin strain rate is equal to the macroscopic strain rate.

Fig. 13. (a) Schematic of the tensile testing specimen (all dimensions are in “mm”). (b) Predicted twin volume fraction in Mg-3Al-0.3Mn alloy as a function of true tensile strain for B = 0.05. (c) and (d): the experimental and predicted flow curves and strain hardening rate plots for Mg-3Al-0.3Mn alloy in tension parallel to the extrusion direction for B = 0.05, σ_0 = 142 MPa, σ_{sat} = 229 MPa, h_m = 2400 MPa, n = 0.56, while h_t was varied from 10 MPa to 8000 MPa.

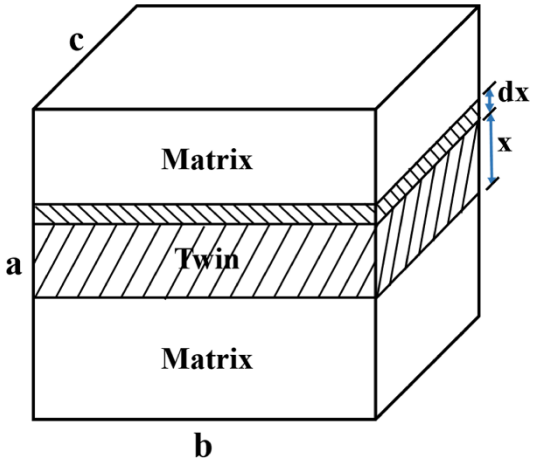

Fig. 1. Schematic representation of the matrix and twin phases in a grain showing the growth of a twin.

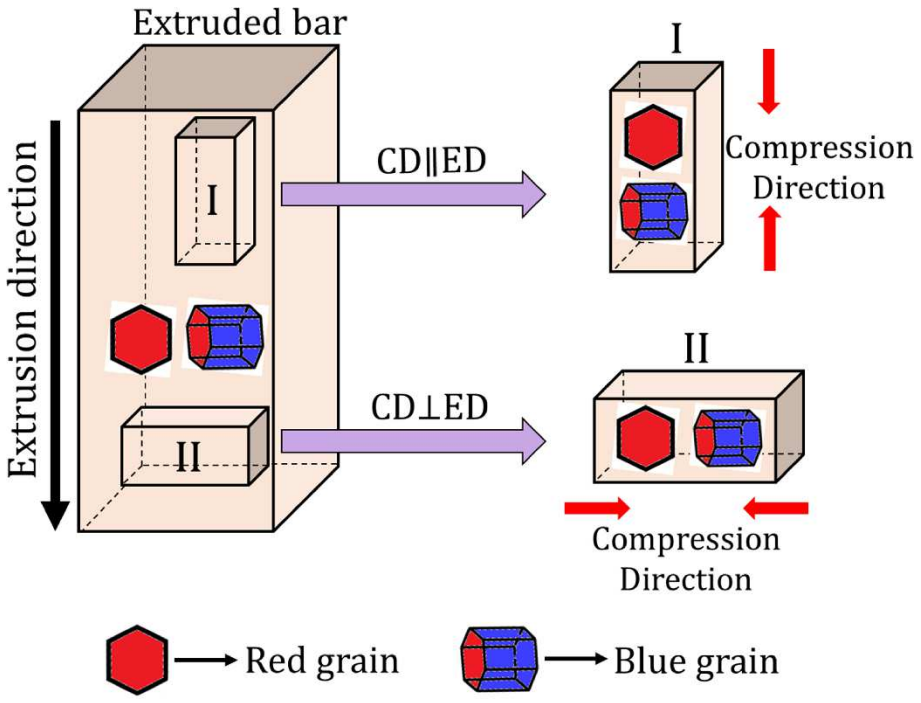

Fig. 2. Sample geometry and testing directions showing the extruded bar from where the samples were machined for CD∥ED marked as I and CD⊥ED marked as II. The hexagonal unit cell shows the orientation of the main texture components.

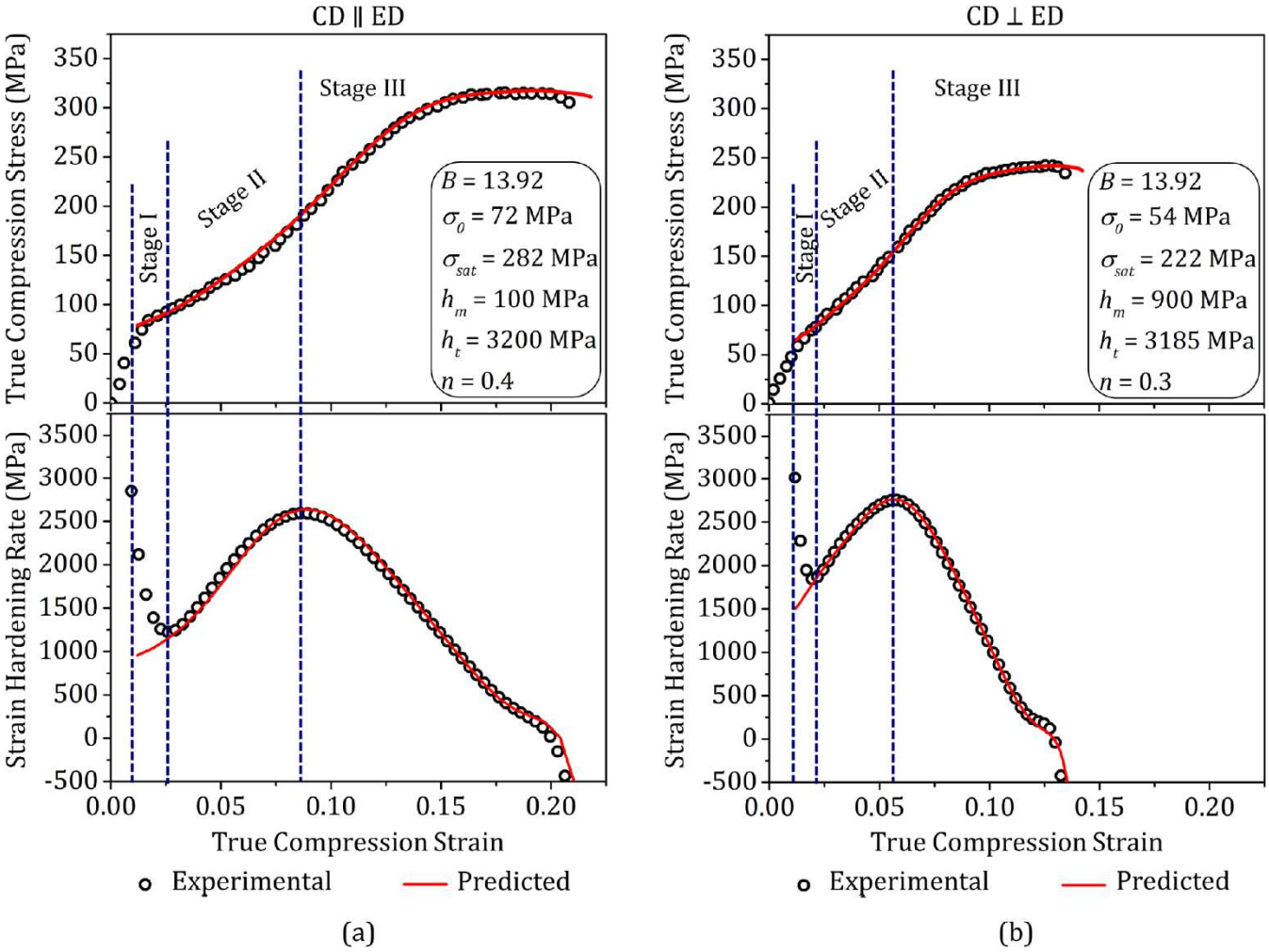

Fig. 3. Experimental and predicted flow curves and strain hardening rate plots of Mg-3Al-0.3Mn alloy during uniaxial compression test carried out (a) parallel and (b) perpendicular to the extrusion direction of the original bar.

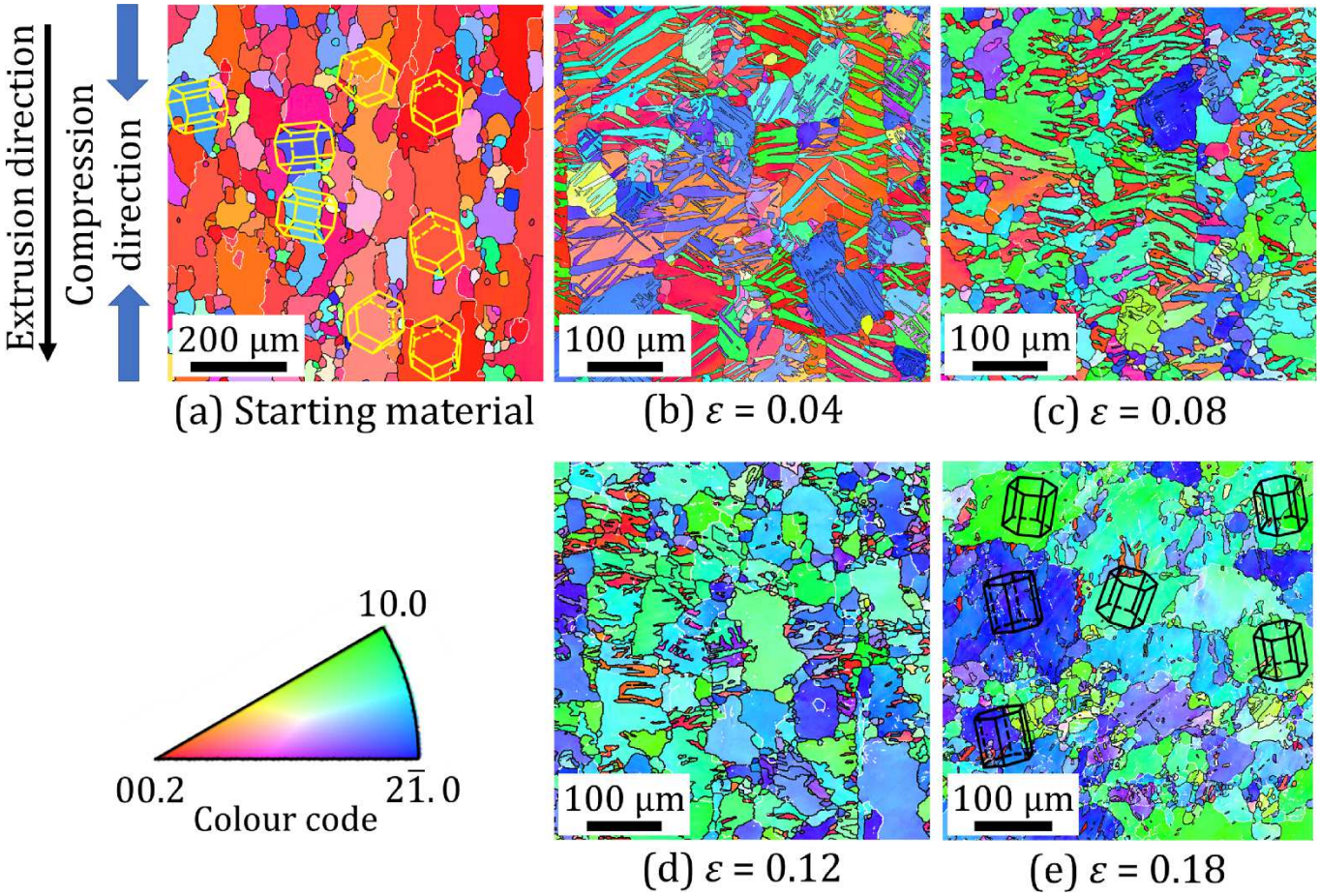

Fig. 4. Measured inverse pole figure (IPF) maps of the Mg-3Al-0.3Mn alloy with compression direction parallel to the extrusion direction. (a) as-received extruded material, and deformed samples to strains of: (b) 0.04, (c) 0.08, (d) 0.12 and (e) 0.18. The hcp unit cells are superimposed on the initial and final states. The colour key code represents the direction normal to the map in the crystal reference system of the grains.

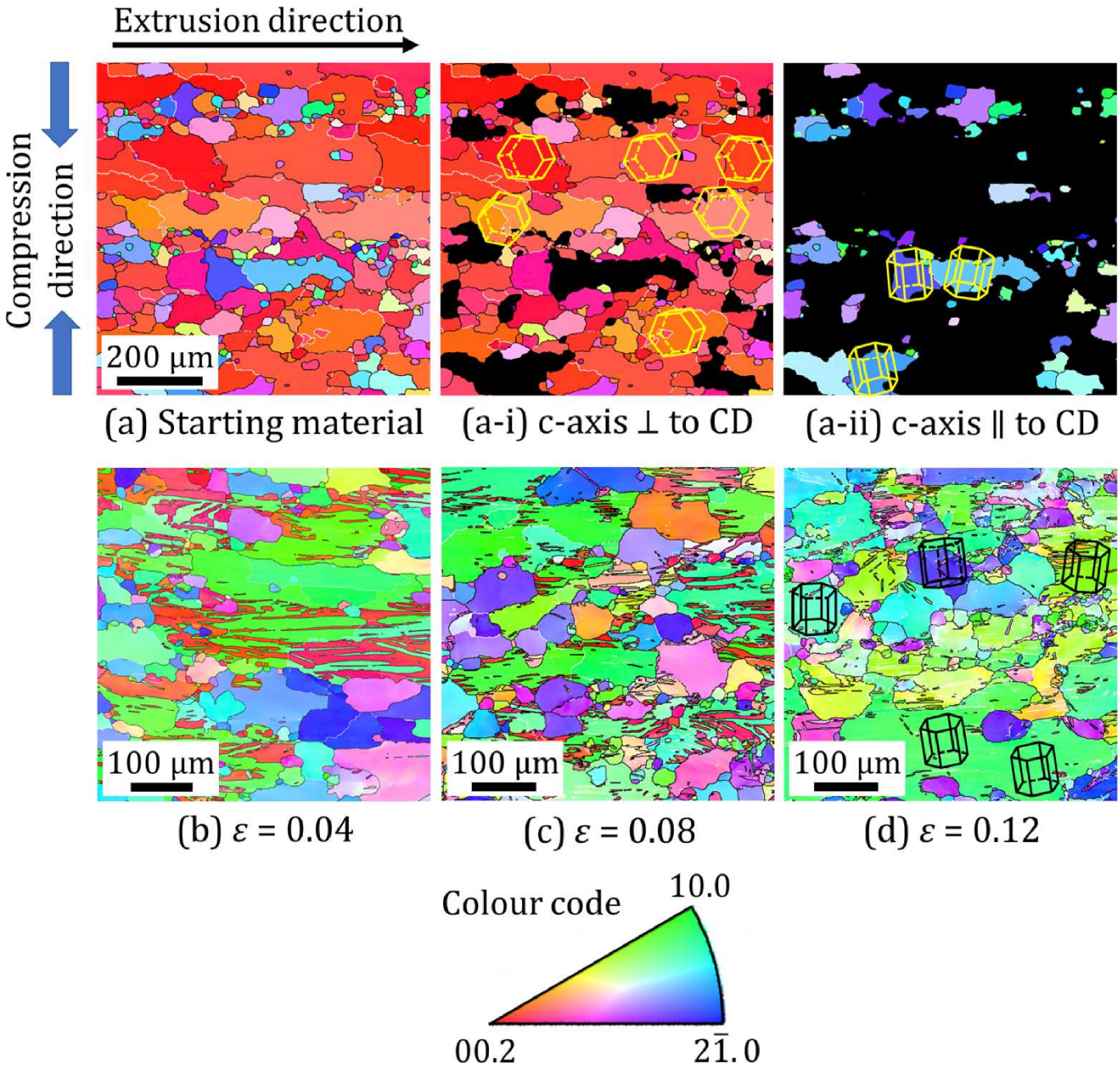

Fig. 5. IPF maps of Mg-3Al-0.3Mn alloy measured after compression perpendicular to the original extrusion direction. (a)-(a-i)-(a-ii): as-received extruded material showing the full microstructure in (a) and its partitioned microstructures in (a-i)-(a-ii). (a-i) shows grains with c-axis near perpendicular to CD while (a-ii) displays grains with c-axis parallel to CD. The deformed states are shown as a function of strain for (b) ε = 0.04, (c) ε = 0.08 and (d) ε = 0.12. Some hcp unit cells are superimposed in (a-i), (a-ii) and (d) for showing the characteristic orientations of the grains. The colour key code represents the direction normal to the map in the crystal reference system of the grains.

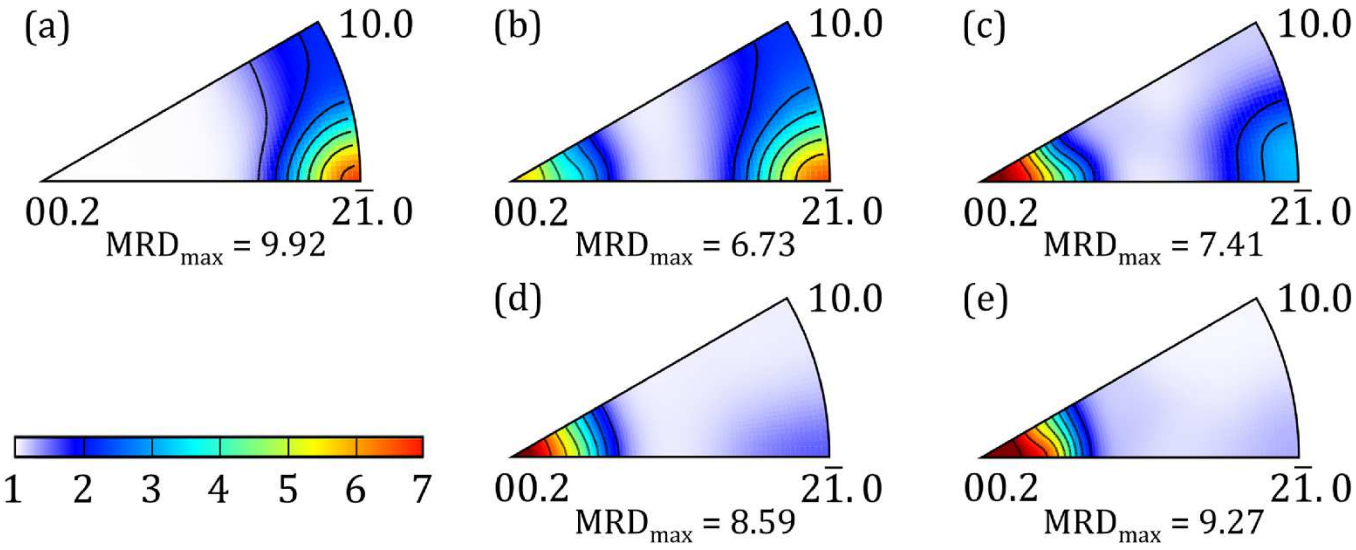

Fig. 6. Inverse pole figures of the CD axis in Mg-3Al-0.3Mn alloy for loading CD∥ED. (a) as-received, and compression tested samples up to intermediate strains of (b) 0.04, (c) 0.08, (d) 0.12 and (e) 0.18. The colour bar represents the multiples of random distribution (MRD).

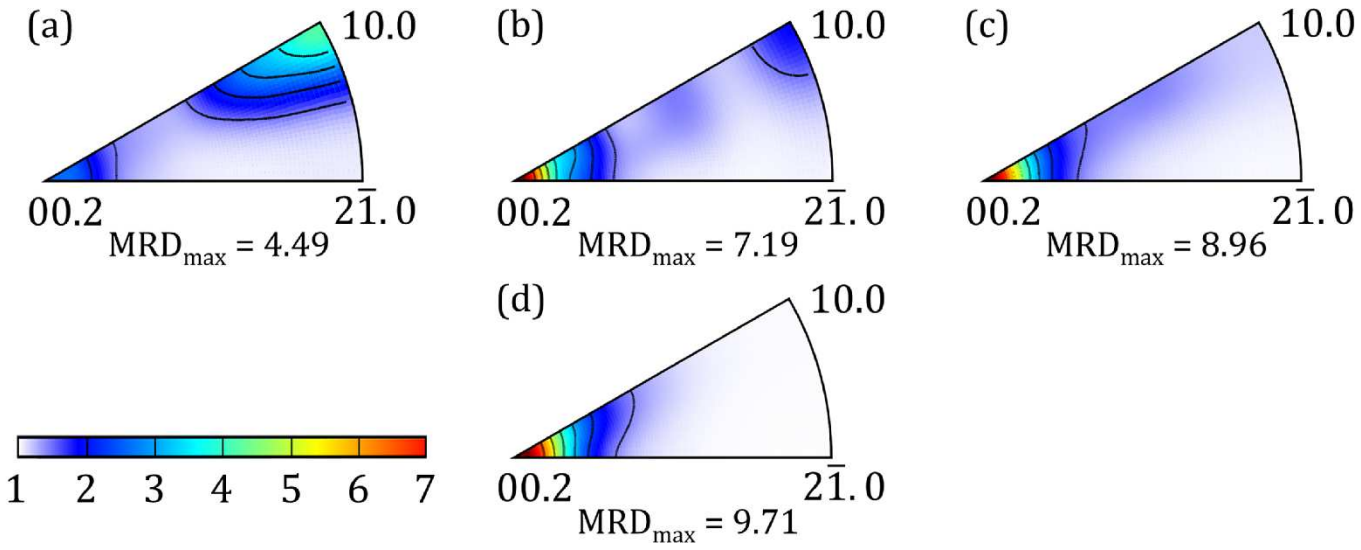

Fig. 7. Inverse pole figures of the CD axis in Mg-3Al-0.3Mn alloy for loading CD⊥ED. (a) as-received, and compression tested samples up to intermediate strains of (b) 0.04, (c) 0.08 and (d) 0.12. The colour bar represents the multiples of random distribution (MRD).

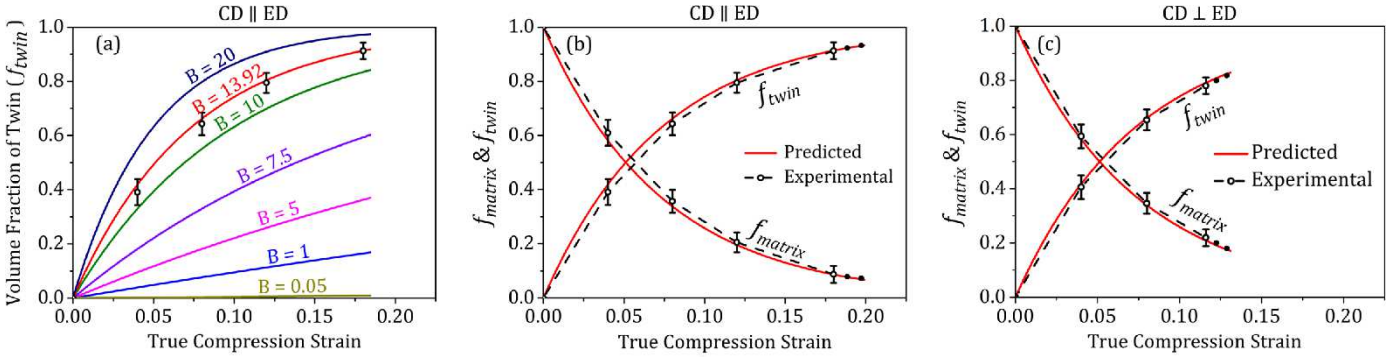

Fig. 8. (a) Calibration of the *B* parameter for predicting the twin-volume fraction in Mg-3Al-0.3Mn alloy as a function of compression strain. The open circle markers represent the experimental twin volume fractions for the CD∥ED case. *B* = 13.92 was identified for both the (b) CD∥ED and (c) CD⊥ED loadings.

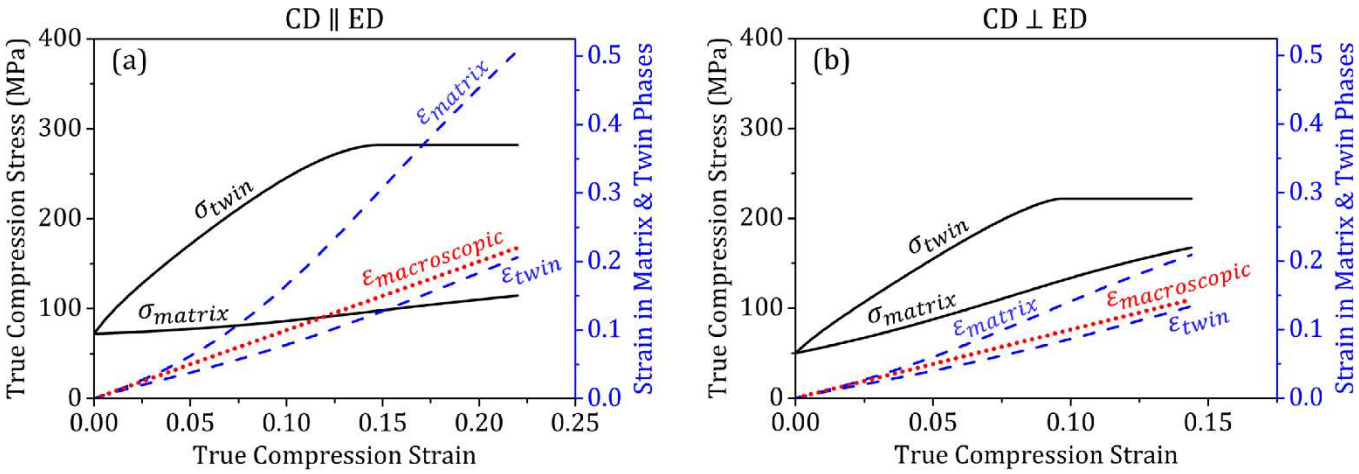

Fig. 9. Predicted variations of the stresses and strains for the matrix and the twin phases as a function of true compression strain for (a) CD∥ED and (b) CD⊥ED. The red dotted line represents the macroscopically imposed strain.

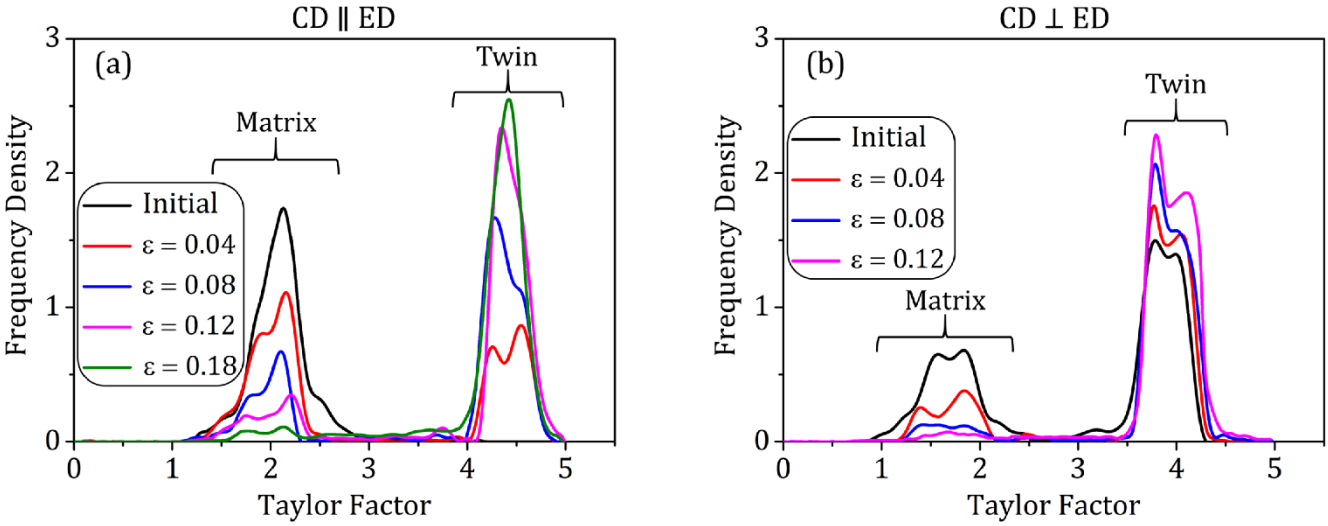

Fig. 10. Taylor factor distribution plots for the initial as well as for the deformed samples for (a) CD∥ED and (b) CD⊥ED.

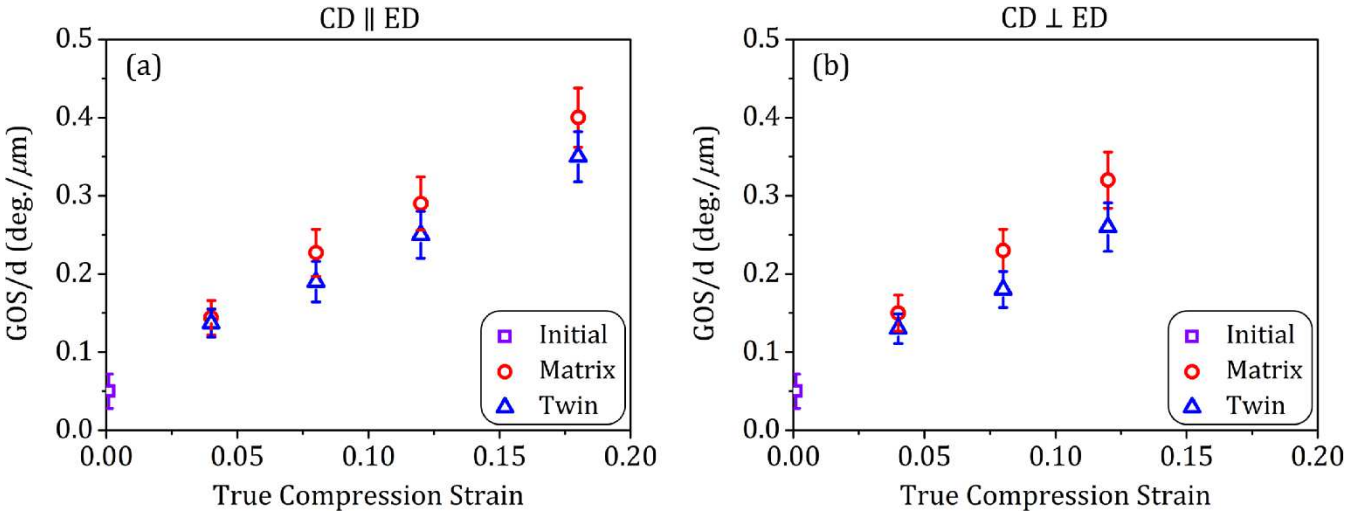

Fig. 11. Average Grain Orientation Spread (GOS) divided by the grain diameters (d) obtained from the experimental microstructures for the initial and deformed samples of the Mg-3Al-0.3Mn alloy for the (a) CD∥ED and (b) CD⊥ED cases.

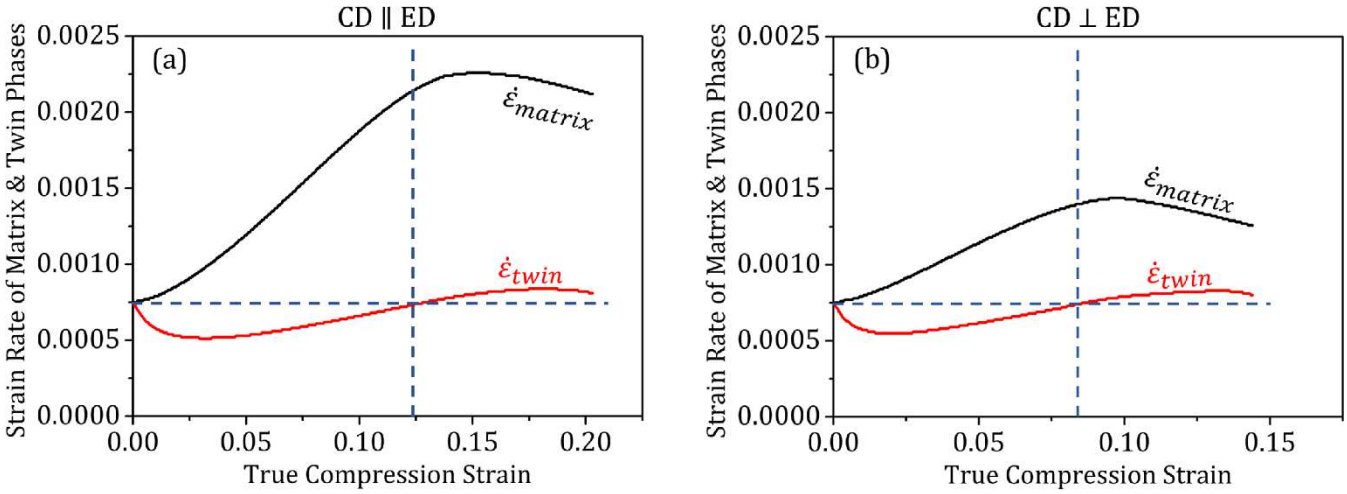

Fig. 12. Predicted strain rate partitions in the matrix and the twin phases as a function of strain for (a) CD∥ED and (b) CD⊥ED. Horizontal dashed line represents the macroscopic strain rate and the vertical dashed line represents the position where the twin strain rate is equal to the macroscopic strain rate.

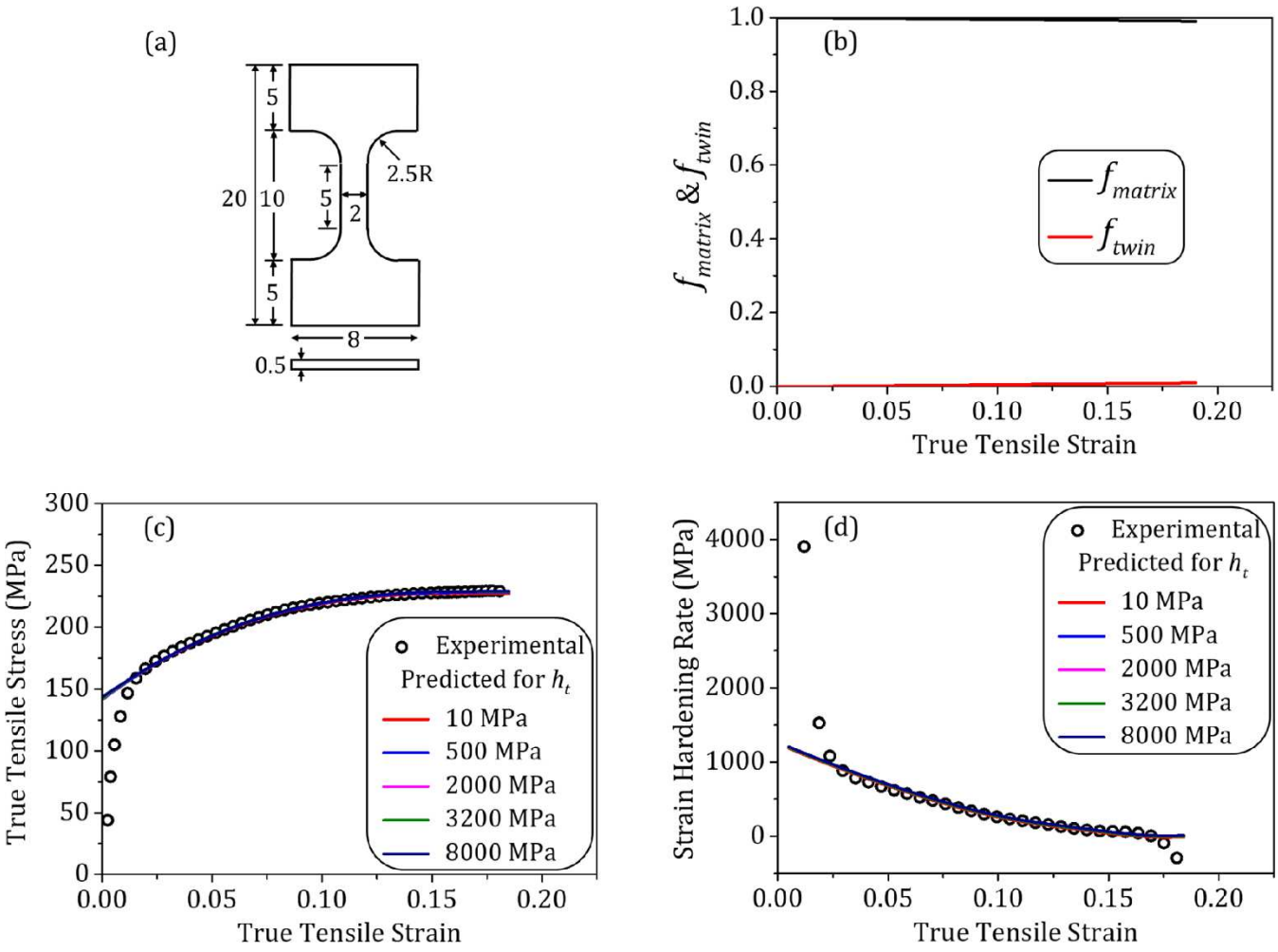

Fig. 13. (a) Schematic of the tensile testing specimen (all dimensions are in "mm"). (b) Predicted twin volume fraction in Mg-3Al-0.3Mn alloy as a function of true tensile strain for $B = 0.05$. (c) and (d): the experimental and predicted flow curves and strain hardening rate plots for Mg-3Al-0.3Mn alloy in tension parallel to the extrusion direction for $B = 0.05$, $\sigma_0 = 142$ MPa, $\sigma_{sat} = 229$ MPa, $h_m = 2400$ MPa, $n = 0.56$, while h_t was varied from 10 MPa to 8000 MPa.

Table 1. The identified parameter values for the analytical model for the two sample orientations in compression.

Testing	σ_0	σ_{sat}	h_m	h_t	n
CD∥ED	72 MPa	282 MPa	100 MPa	3200 MPa	0.4
CD⊥ED	54 MPa	222 MPa	900 MPa	3185 MPa	0.3

Table 2. The average Taylor factors obtained in axisymmetric compression for the IPF maps as a function of strain.

Testing	$\varepsilon = 0$	$\varepsilon = 0.04$	$\varepsilon = 0.08$	$\varepsilon = 0.12$	$\varepsilon = 0.18$
CD∥ED	2.46	2.83	3.28	3.51	3.88
CD⊥ED	2.68	3.04	3.46	3.79	-

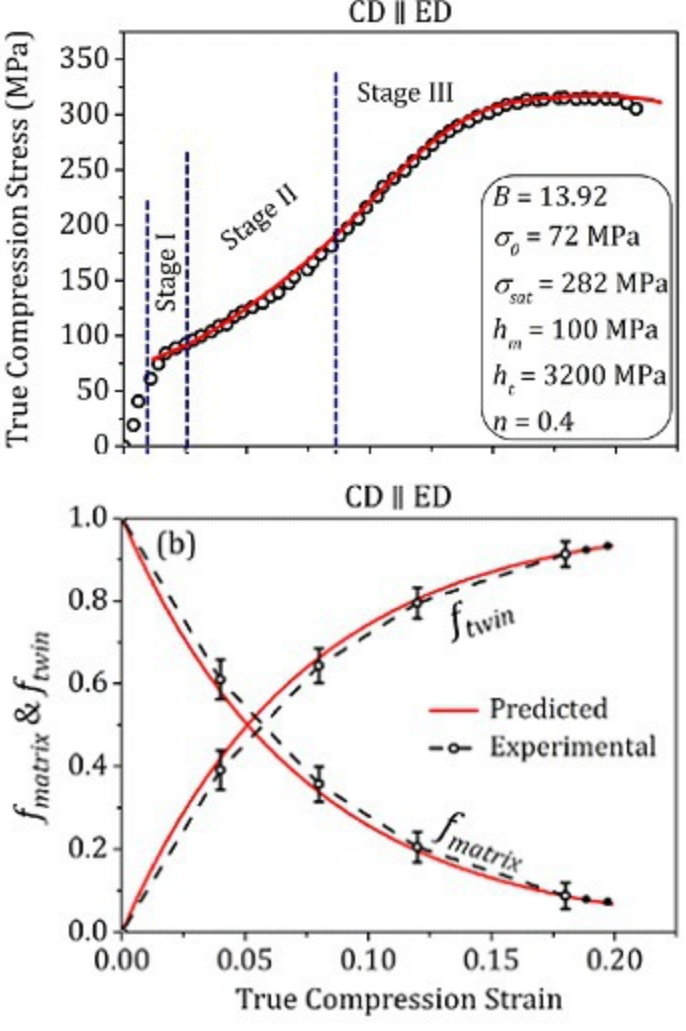
CD ∥ ED
True Compression Stress (MPa)
350
300
250
200
150
100
50
0
Stage I
Stage II
Stage III
B = 13.92
σ0 = 72 MPa
σsat = 282 MPa
hm = 100 MPa
ht = 3200 MPa
n = 0.4
CD ∥ ED
(b)
fmatrix & ftwin
1.0
0.8
0.6
0.4
0.2
0.0
ftwin
Predicted
Experimental
fmatrix
0.00
0.05
0.10
0.15
0.20
True Compression Strain